3-28-2005

The Effects Of Moisture On Thin Film Delamination And Adhesion

Patrick Waters
University of South Florida

The Effects Of Moisture On Thin Film Delamination And Adhesion

by

Patrick Waters

A thesis submitted in partial fulfillment
of the requirements for the degree of
Masters of Science in Mechanical Engineering
Department of Mechanical Engineering
College of Engineering
University of South Florida

Major Professor: Alex Volinsky, Ph.D.
Thomas Eason, Ph.D.
Autar Kaw, Ph.D.

Date of Approval:
March 28, 2005

Keywords: Copper, Diamond like Carbon, Nanoindentation, Environmentally Assisted Fracture

DEDICATION

To my parents, this would not have been possible without their support.

ACKNOWLEDGEMENTS

I would like to thank my advisor Dr. Alex Volinsky for his support and guidance throughout my research. I am very grateful for the help and advice my committee members Dr. Eason and Dr. Kaw have given me since my days as an undergraduate. I would also like to thank the rest of the faculty and staff in the mechanical engineering department for being a friendly and positive influence. I want to acknowledge Seagate for providing samples and a special thanks to NACE for funding my research.

TABLE OF CONTENTS

LIST OF TABLES

LIST OF FIGURES

THE EFFECTS OF MOISTURE ON THIN FILM DELAMINATION AND ADHESION

Patrick Waters

ABSTRACT

Significant drops in adhesion have been measured for copper and diamond like carbon (DLC) films with the introduction of water at the film/substrate interface. A 1 μm thick tungsten superlayer with high compressive residual stress was deposited on the films of interest to help induce interfacial debonding by indentation. Modifications were made to the superlayer indentation technique to introduce water at the interface while performing indents. Film adhesion dropped by a factor of 10 to 20 for the copper films and 50 to 60 for the DLC films. The reduction in adhesion is believed to be caused by a combination of lowering surface energy and a chemical reaction at the crack tip. When the film compressive residual stress is at least 4 times the critical buckling stress of a debonded film, telephone cord delaminations morphology can be observed. Delamination propagation has been induced in the past by applying a mechanical force to the film and similar results have been observed with the introduction of water. Crack propagation rates of 2 to 3 microns per second were measured for the DLC films with the introduction of water at the film/substrate interface. Telephone cord delaminations show potential for future use as microchannels in microfluidic devices and have shown excellent stability when manipulated with a microprobe to control fluid transport.

CHAPTER 1

INTRODUCTION

1.1 Thin film technology

Thin films can be found everywhere, from the paint on a car to the interconnects in the computer processor. There is an endless variety of applications based on the various functional properties of thin films. Some applications include thin films used in information storage, optics, microelectronics and in biomedical fields. These applications are possible because of the thin films' magnetic, reflective, electrical, mechanical and other properties. Whenever thin films are to be applied, certain mechanical properties such as modulus and hardness need to be known for design specifications. Generally the bulk material properties cannot be used for predicting the mechanical properties of a thin film. A major contributor in influencing the mechanical properties of thin films will be the method and parameters used for its deposition.

Just as there are thousands of bulk materials to choose from, there are just as many types of thin films. Thin films can be metallic, ceramic, polymer or even metallic glass to list a few. Many tests have been performed to measure the mechanical properties and adhesion of these different types of thin films [1-4]. Some common methods for depositing the various types of thin films are electroplating, chemical vapor deposition (CVD) and physical vapor deposition (PVD) [5]. Regardless of what process is used for

deposition or what application the thin film is being used for, good film adhesion is usually required.

The motivation behind this research is to measure the effects of a wet and potentially corrosive environment on film adhesion and compare those values to the adhesion measurements taken in a dry environment. With the growing number of uses for thin films, there will be an increase in the variety of environments in which these thin films will be operating.

1.2 Adhesion

Adhesion can be described as the mechanical strength or bond strength between two joined bodies. To separate the two bodies an external force must be introduced. Adhesion is believed to be caused by a few different reasons: atomic bonds created by the interaction of the two surfaces which is thought to be the primary contributor, mechanical locking and friction due to surface texture and a transition layer produced by the diffusion of one material into the other [6]. From a thermodynamic perspective, the true work of adhesion at the interface is the amount of energy required to create free surfaces from the bonded materials. The ideal case where the true work of adhesion can be defined is when brittle fracture occurs and there is no energy dissipated due to plastic deformation. All energy is conserved as new surfaces are formed:

$$W_A = \gamma_f + \gamma_s - \gamma_{fs} \quad (1),$$

where γ_f is the surface energy of film, γ_s is the surface energy of the substrate and γ_{fs} is the interfacial energy.

The interfacial energy can be found by knowing the surface energies of the film and substrate and using the contact angle technique schematically presented in Figure 1:

$$\gamma_{fs} = \gamma_s - \gamma_f \cos\Theta \qquad (2),$$

where Θ is the contract angle between the droplet free surface and the substrate. If Θ is less than 90º, the liquid is said to wet the surface. If Θ is greater than 90º, the cohesive forces in the liquid are greater than the adhesive forces of the liquid to the surface and the liquid is non-wetting. Usually the term surface tension is used for liquids and the term surface energy is used for solids. Water has a surface tension of 72 dynes/cm^2 at 25º C, and decreases with temperature increase. Adding impurities like soap or detergent will also decrease the surface tension of water, "wetting it out" so that is can penetrate smaller pores making it a more efficient cleaner. The Sessile drop method can be used for finding the surface energy of solids [7].

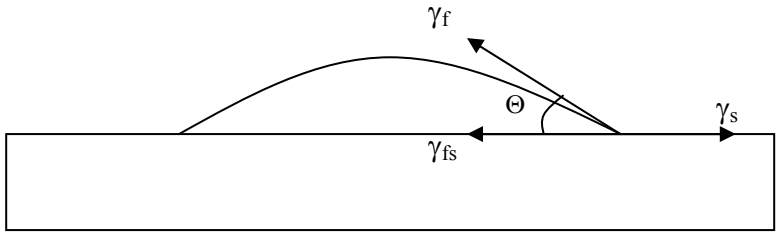

Figure 1. Contact angle technique.

The contact angle technique is performed by placing a drop of a liquid of known surface tension on the test surface and illuminating it through a moveable eyepiece. The eyepiece is connected to an electronic protractor which displays the viewing angle. The device is constructed so that when the viewing angle equals the contact angle, the

illumination viewed through the eyepiece is maximized. The contact angle and the surface tension of the liquid can then be used to calculate the surface energy of the substrate [7].

The dyne pen is another method for measuring the surface energy for either the film or the substrate [7]. This method involves the use of a set of commercially available felt-tip pens containing a range of inks with a known surface tension. One of the pens is used to apply a thin film of ink over approximately 7 square centimeters of the test surface. If the ink film breaks into droplets in less than two seconds, the process is repeated again using a pen filled with ink having a lower surface tension. This procedure is used to determine the lowest surface tension ink that forms a continuous film and remains intact for at least two seconds. The value of the surface tension of this ink is then taken as the surface energy of the test substrate [7].

With the surface energies and contact angle known the Young-Dupré equation can be used to find the true work of adhesion:

$$W_A = \gamma_f + \gamma_s - \gamma_{fs} = \gamma_f (1 + \cos\Theta) \qquad (3).$$

Lipkin and others measured the true work of adhesion of a gold thin film on a sapphire substrate to be approximately 0.9 J/m^2, which corresponds to the typical values of 1-2 J/m^2 for the true work of adhesion measured for metal films on ceramic substrates [8].

In a perfect situation we could say that the true work of adhesion is equal to the film/substrate adhesion. This follows the idealized case of Griffith fracture where the fracture resistance Γ_i, is assumed to be equal to the thermodynamic (true) work of adhesion W_A. The true work of adhesion does not account for energy loss due to plastic

deformation or friction. Even as fracture occurs in a brittle material there will always be a small plastic zone that ahead of the crack tip radius that may extend from a single bond to over several atomic spacings [9, 10]. The small nonlinear plastic zone immediately surrounding the crack tip will be followed by a linear elastic zone that serves the function of transmitting the applied stresses to the inner regions. A more sensible value of adhesion is the practical work of adhesion:

$$W_{A,P}(W_A) = W_A + U_f + U_s \quad (4),$$

where W_A is still the true work of adhesion, U_f is the energy per unit area spent due to plastic deformation in the film and U_s is the energy per unit area spent due to plastic deformation in the substrate. The practical work of adhesion $W_{A,P}$, is also called the interfacial toughness or the resistance to crack propagation of the film and substrate pair. The practical work of adhesion is more conducive for analyzing fracture in metal films and will be used as the adhesion measurement in this thesis.

1.3 Fracture criterion

Now that the basic definitions of adhesion are established, fracture mechanics will be considered. In 1920 Griffith formulated that a crack will continue to grow as long as the strain energy release rate (G) from the surrounding elastically strained material exceeds the energy required to form new surfaces [11]:

$$G \geq \Gamma_i \quad (5),$$

where G is the strain energy release rate and Γ_i is the material's resistance to crack growth. G is frequently referred to as the mechanical energy release rate and it is defined as [12]:

$$G = -\frac{dU_M}{dA} \quad (6),$$

where A is the crack area and dU_M is the total mechanical energy change associated with the crack propagation. The total mechanical energy change can be broken into two parts and is defined as:

$$dU_M = dU_E + dU_A \quad (7),$$

where dU_A is the change in energy of the applied loading system and dU_E is the change in elastic strain energy.

The change in elastic energy can be described for two conditions: the fixed grips or the constant load conditions. Under fixed grips condition the applied loading system suffers zero displacement as the crack extends (u_0 = constant) and the elastic strain energy will decrease with crack extension. With fixed grip conditions:

$$u_0 = const$$

$$dU_E = -\frac{1}{2}\frac{u_0^2}{\lambda^2}d\lambda \quad (8),$$

where $\lambda=\lambda(c)$ is the elastic compliance.

The second, constant load condition, is where the elastic strain energy increases with a constant load:

$$P = const$$

$$dU_E = \frac{1}{2}P^2 d\lambda \quad (9),$$

Since G does not depend on the loading type the strain energy release rate can be defined as the rate of change of stored elastic strain energy with respect to the crack area under fixed grips conditions:

$$G = -\left(\frac{\partial U_E}{\partial A}\right)_{u_0} \qquad (10),$$

Other methods for evaluating G follow the crack stress field analysis and the next few equations are classic equations for a straight crack of length 2a:

$$K_I = \sigma_{yy}\sqrt{\pi a} \qquad K_{II} = \sigma_{xy}\sqrt{\pi a} \qquad K_{III} = \sigma_{yz}\sqrt{\pi a} \qquad (11),$$

where K is the stress intensity factor for mode I (opening mode), mode II (shear mode), mode III (twisting mode) and σ is the stress field at the crack tip and a is the crack length. Modes one, two and three describe how the loads are being applied to the crack. Figure 2 represents the different modes of fracture and if the stress intensity factor K is greater then the critical stress intensity factor K_c, the crack will propagate.

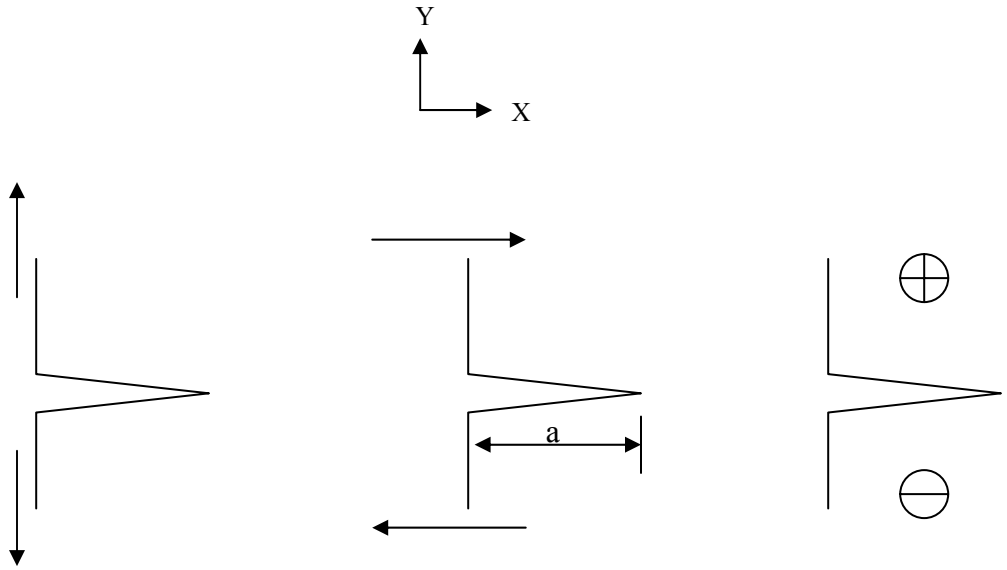

Figure 2. Modes of fracture: a) Mode I b) Mode II c) Mode III.

The Griffith and stress intensity approaches were combined by Irwin [9]:

$$G = \frac{K_I{}^2(1-\nu^2) + K_{II}{}^2(1-\nu^2) + K_{III}{}^2(1+\upsilon)}{E} \qquad (12),$$

where E is Young's Modulus and v is Poisson's ratio of the bulk material.

When making the transition from fracture in bulk materials to thin films, additional effects must be taken into account in order to predict the fracture path. For thin films, the fracture path will depend on interfacial fracture toughness, residual stresses present in the film, mismatches of modulus between film and substrate and the phase angle Ψ. For weakly bonded materials the film/substrate interface will likely be the path of fracture. Because of the mode mixity, the interfacial toughness of the film and substrate varies with Ψ, seen in Figure 3. For one-dimensional blisters, the phase angle defining the relative contributions of normal mode I and shear mode II loads are given by [13]:

$$\tan\Psi = \frac{K_{II}}{K_I} = \frac{4\cos\omega + \sqrt{3}\xi\sin\omega}{-4\sin\omega + \sqrt{3}\xi\cos\omega} \tag{13},$$

where ξ equals δ/h, δ is the blister height, h is the film thickness (Figure 4) and ω is a dimensionless function of the Dundurs' parameters, α and β, which describe the elastic mismatch between the film and substrate. The Dundurs parameters for plane strain are [14]:

$$\alpha = \frac{(\mu_1/\mu_2)(1-\upsilon_1)-(1-\upsilon_2)}{(\mu_1/\mu_2)(1-\upsilon_2)+(1-\upsilon_1)}$$

$$\beta = \frac{1}{2}\frac{(\mu_1/\mu_2)(1-2\upsilon_2)-(1-2\upsilon_1)}{(\mu_1/\mu_2)(1-\upsilon_1)+(1-\upsilon_2)} \tag{14},$$

where μ and v are shear modulus and Poisson's ratio, and the subscripts 1 and 2 refer to the upper and lower bimaterial layers.

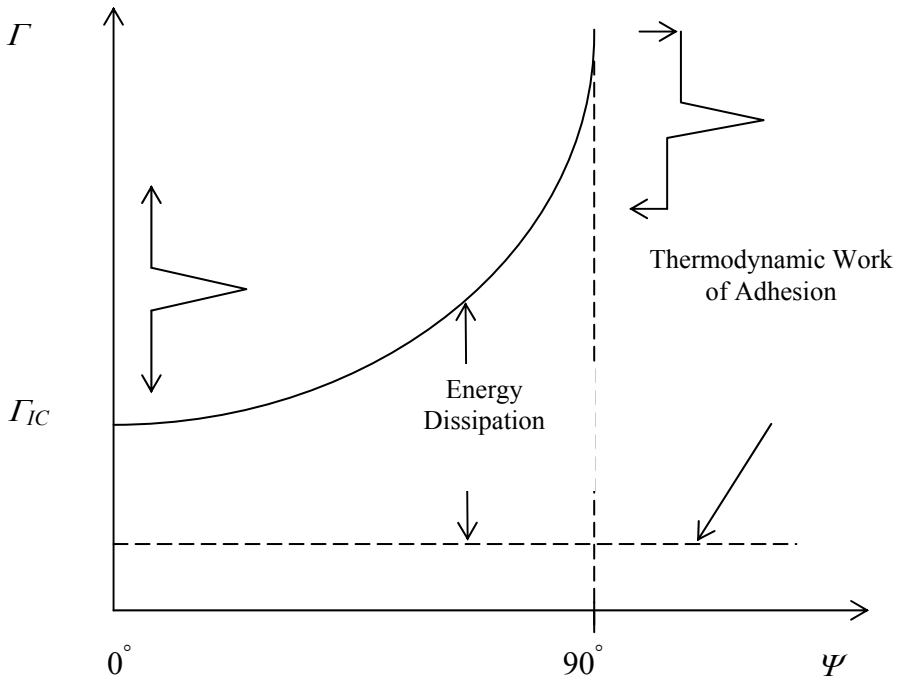

Figure 3. Strain energy release rate as a function of Ψ.

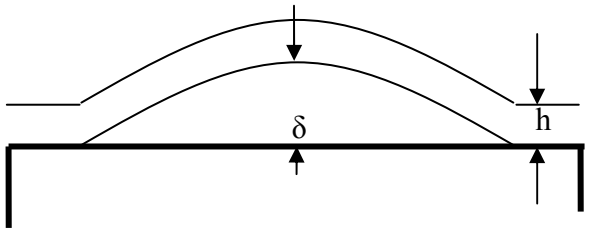

Figure 4. Blister dimensions.

1.4 Literature review

Fracture mechanics in bulk materials have been well documented, and in recent years, has evolved into topics related to thin films and multilayers. The following publications and research results have influenced the direction of this thesis and has raised some unanswered questions which are going to be discussed in the later chapters.

1.4.1 Environmentally assisted fracture

Stress-corrosion cracking (SCC) has been studied in bulk materials, but not as extensively in thin films. Traditionally, SCC in bulk materials is defined as the combination of tensile stress and a corrosive environment. Tensile stress is not always the only stress acting on a structure. The stresses involved can also be compressive, as a result of thermal stresses, residual stresses, and even the corrosion process itself. Stresses induced by the corrosion process are caused by the corrosion products which take up more volume than the initial material. That increase in volume creates residual stresses. Instead of grouping all these cases under SCC, the term environmentally assisted fracture is used.

Common examples of environmentally assisted fracture appear in steel bridges, steam engines, gas pipelines and heat exchangers [15]. All of the aforementioned are structures under large loads in wet and corrosive environments. Failures in bulk materials and structures are usually the result of an overload due to a loss in cross-sectional area. Fortunately, extensive corrosion only takes place under certain combinations of materials and environment. In the early stages, environmentally assisted fractures have cracks on the microscopic level, which may not immediately lead to catastrophic failure in bulk materials, but can lead to failure or delamination in the case of thin films.

1.4.2 Water vapor effects on soda-lime glass fracture

Static fatigue of glass was discovered in 1899 by Grenet [16], who observed the effects of loading rate and time on the glass strength. Glass loaded at rapid rates or used to support a given load for a short period of time was relatively strong. When it was

loaded at a slower rate or forced to support a given load for a longer time the glass was relatively weak [16]. Over the next 30-40 years many authors had summarized the experimental and theoretical results of static fatigue tests. The main belief was that static fatigue was a result of exposure to the atmosphere, primarily a stress-dependent chemical reaction between water vapor and the surface of glass. When water vapor is able to penetrate into the small cracks within the glass, the cracks lengthen and failure occurs when the crack tip is long enough to meet the Griffith fracture criterion.

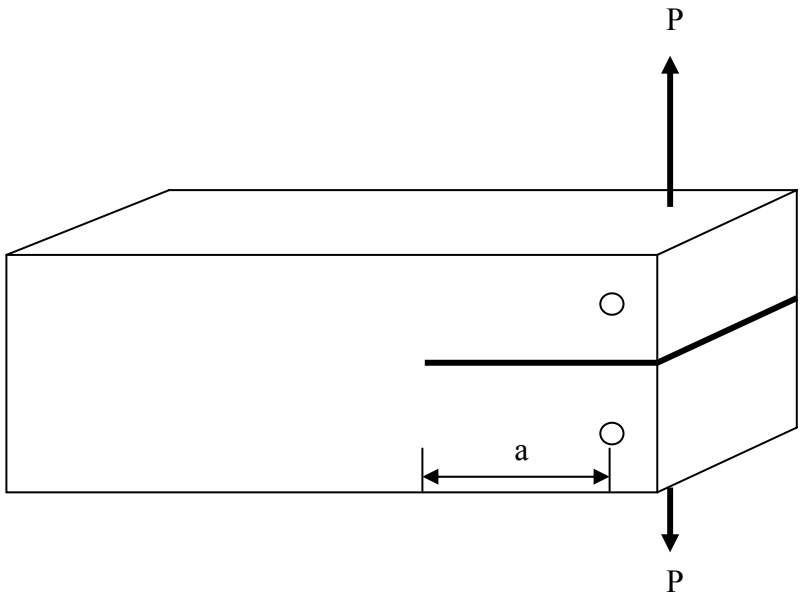

Figure 5. Schematic of double cantilever cleavage test.

In 1967 Wiederhorn ran tests to further explain the results observed in glass failure. Using a double cantilever cleavage arrangement seen in Figure 5, a constant load was applied and the crack velocity was measured as a function of the applied load and relative humidity. Results showed that the crack motion is complex and depends on the amount of moisture in the air [17]. Three regions of motion were identified and their

trend has been recreated in Figure 6. The crack velocity is plotted against the applied load and for each of the runs the relative humidity was varied.

Region I is the initial steep line on the log scale. Region II is the portion of the lines that appear to plateau. Region III is where all the runs come together into another steep line. In region I the crack velocity is exponentially dependant on the applied load. For region II the crack velocity is nearly independent of applied load and the position of each curve shifts to lower velocities as the water amount in the environment decreases. In region III the crack velocity again exponentially depends on the applied load. Wiederhorn derived equations to fit the data in regions I and II, but was unsuccessful for predicting the trend in region III.

The velocity of crack propagation in region I is predicted by:

$$v = (0.0275 a x_0^n \exp bP) / n \qquad (15),$$

where a and b are constants taken from the rate law:

$$N = a x^n e^{bP} \qquad (16),$$

where N is the number of moles of water per unit area per unit time reacting at the surface, x is the mole fraction of water in the nitrogen next to the crack tip, P is the applied load and n is the order of the chemical reaction.

For region II the velocity of crack motion is predicted by:

$$v^+ = 0.0275 c D_{H_2O} x_0 / \delta n \qquad (17),$$

where D_{H2O} is the diffusion coefficient of water vapor to crack tip and δ is the thickness of the boundary layer of nitrogen next to the crack tip.

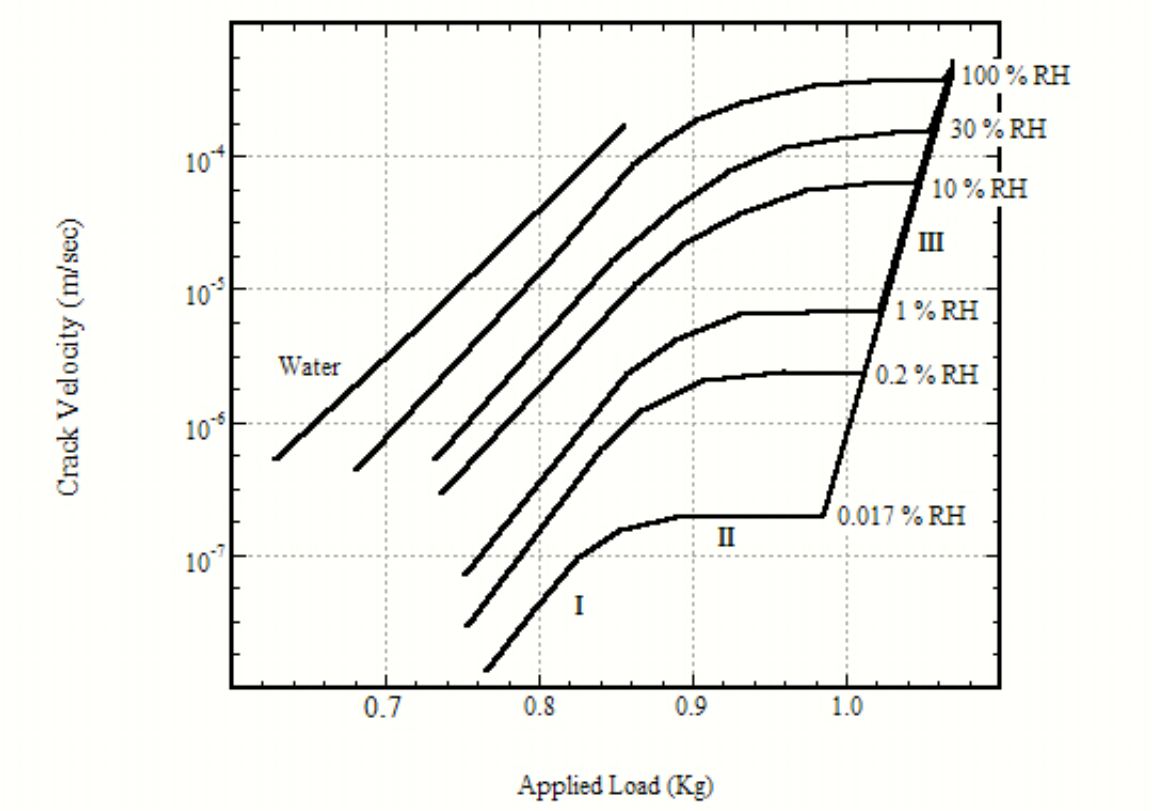

Figure 6. Dependence of crack velocity on relative humidity adapted from Wiederhorn' experiments [17].

1.4.3 Moisture effects in thin films

In addition to moisture effects in bulk glass, environmental degradation of adhesion has been considered for silver, low-k dielectric, boron nitride and silicon dioxide films [18-23]. In the late 1970's Sandia Laboratories conducted tests in order to explain the deterioration of the silver/glass interface in second surface solar mirrors. The choice of second surface silvered glass for mirror applications was primarily due to the durability of glass and the high reflectivity of the silver. The defects that appeared in the solar mirrors are similar in appearance to those shown in Figure 7. Figure 7 is a picture of an early nineteenth century mirror held at The Art Institute of Chicago. In order to

reproduce the effects of aging, tests were performed at an elevated temperature of 65ºC and high humidity of 95%. A few of the final conclusions are listed below [18]:

1) Water intrusion into the mirror module was arranged in such a way as to recreate standing water in contact with the mirror's backing paint for long periods of time.
2) Water penetration through the paint layer via a diffusion and/or wicking action is enhanced somewhat by the presence of contaminants picked up from the organic materials in the module. These contaminants can act to lower the surface tension of the water and allow more rapid penetration through the pores in the paint.
3) Delamination of the silver layer by an as yet undefined process.

Tests from Sandia labs showed that there may be more than one mechanism at work, including the type of paints used on the back of the mirror, but the primary one was due to the presence of water. Recent conclusions regarding other types of thin films indicate that Sandia National Laboratories correctly concluded that water was a key factor in the deterioration of the solar mirrors.

Figure 7. Delamination of silver backing on a mirror.

Vlassak and colleagues at Harvard University have been studying environment effects on the fracture of organosilicate glass (OSG) thin films. OSG thin films are one of the leading candidates among new dielectric materials being considered for microelectronics. The presence of –CH3 groups makes the OSG films very porous and less dense than the fused silica. Additionally, with their mechanical properties being inferior, there is a concern for the possibilities of delamination during processing [19]. Through the use of the four-point bending technique, subcritical crack growth was studied and the strain energy release rates and the average crack growth rates were evaluated. Results showed that with increasing relative humidity, the stress-corrosion thresholds shift to lower values of *G*. It was also recorded that an increase in pH of the solution results in a significant increase in crack velocity and decreasing adhesion [20, 21]. Similar effects were seen in other films.

The cubic phase of boron nitride (cBN) is one of the hardest materials known and for that reason it has potential in thin film wear resistant applications. Due to the deposition parameters needed to obtain a cBN film, high compressive residual stress of 5-20 GPa is typically seen. Frequently, thicker films experience even higher compressive stress. One result of higher compressive stress is a greater likelihood of spontaneous delamination. It was noted that an increase in relative humidity accelerated the degradation of the thin film.

Stress analysis was initially conducted to examine the potential increase in the residual stress with an accompanying increase in relative humidity. It was noticed that there was a small short term increase in stress. It was not, however, enough to induce delamination. Long term observation indicates a significant decrease in residual stress. The result was caused by delamination of the cBN thin film, which is thought to be triggered by an increase in humidity. Even breathing on the cBN films after delamination had occurred, increased film buckle size by up to 1 μm. The final conclusions drawn from these tests indicate that water has a strong effect on film delamination and that there must be an interaction at the film/substrate interface with water [22].

For PECVD SiO_2 films electrostatic force grips have been applied in tensile tests for measuring humidity effects on their strength. The tensile test and fracture toughness measurements were conducted in both air and in vacuum. The mean strength was measured to be 1.2-1.9 GPa in vacuum and 0.6-1.0 GPa in air [23]. It was concluded that the drop in tensile strength was caused by moisture in the air which is absorbed at the crack tip, therefore increasing crack growth rates.

The preceding work on environmentally assisted fracture illuminates a very clear trend that establishes water as a catalyst to increasing crack growth rates. In the case of thin films, this has resulted in lower adhesion values, which in turn affects the functionality of the thin film. In this thesis quantitative adhesion results are reported showing a significant drop in adhesion with the introduction of water. Considerations on why there is a drop in adhesion will also be discussed.

CHAPTER 2

THIN FILM DEPOSITION AND MECHANICAL CHARACTERIZATION

2.1 Methods for depositing thin films

It was mentioned earlier that deposition processes can influence the mechanical properties and create defects in thin films. For this reason bulk material properties cannot always be used for predicting the mechanical properties of thin films. Some conditions like temperature, pressure and deposition rate can be controlled during the deposition process. These conditions, or parameters can force thin films to settle with a certain crystal orientation or lack thereof, which will effect the mechanical properties of the thin film [5]. Intrinsic stresses can also be a product of the deposition parameters and may lead to cracking or buckling of the thin film. It will be described here how these compressive residual stresses act as an additional stored energy source to facilitate buckling in thin films and will be used in nanoindentation adhesion measurements.

2.1.1 Physical vapor deposition (PVD)

PVD is a method in which atoms are transferred from a source (target) to a substrate in the form of a vapor. It is a very popular method for depositing metals due to the lower temperatures during deposition. When temperatures are high thermal

stress may develop, caused by mismatches in the thermal expansion coefficients of the substrate and the thin film. Two commonly used forms of PVD are sputtering and evaporation.

Sputter deposition was discovered in 1852 by Grove [24]. It produces a thin film by dislodging atoms from the source through the impact of gaseous ions. The substrate is placed in a vacuum chamber with the source material and an inert gas at low pressure usually in the mTorr range. A gas plasma is struck by applying voltage to the target, causing the gas to become ionized, where it then accelerates towards the surface of the target. Atoms are knocked off the target material and condense on the substrate. The basic principle behind sputter depositing is the same for all sputtering technologies. What usually differs between the different types of sputtering methods is the power supply. Some commonly used processes include DC, RF, magnetron and reactive sputtering. The 2400 Perkin-Elmer sputtering system was used for depositing the Cu films tested in this thesis. A typical RF sputtering setup is shown in Figure 8.

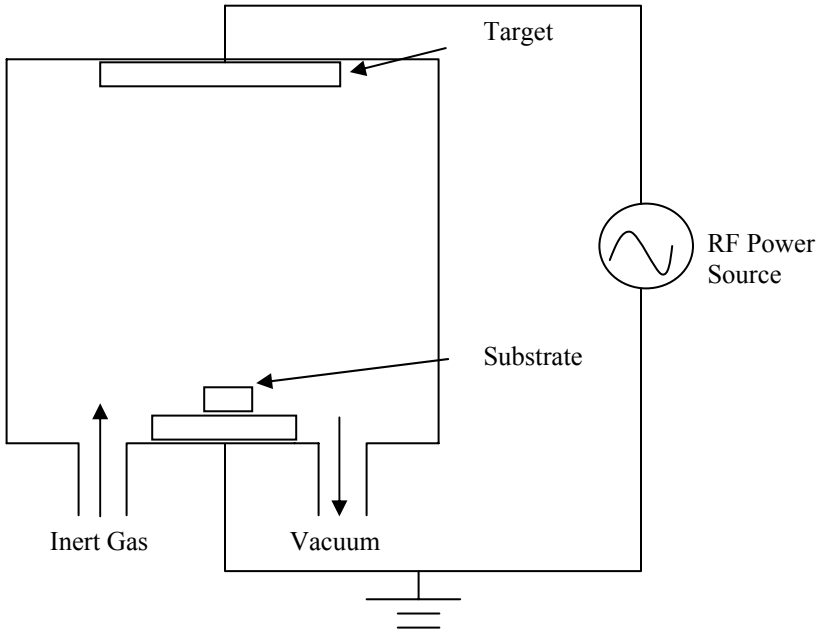

Figure 8. Schematic of a RF sputtering system.

In evaporation deposition, a substrate and source materials are placed inside a vacuum chamber. The source material is heated to the point where it starts to evaporate. The vacuum allows the atoms to evaporate freely in the chamber and condense on the substrate. Like sputter deposition, there are many different types of evaporation, but the basic principles remain the same. The main differences in evaporation deposition methods have to do with the way the source material is heated. Two popular methods for heating the source are electron beam evaporation and resistive evaporation. In e-beam evaporation an electron beam is aimed at the source material causing local heating and evaporation. In resistive evaporation a holder containing the source material is heated by electrical resistance with a high current to evaporate the material.

2.1.2 Chemical vapor deposition (CVD)

In chemical vapor deposition the substrate is placed inside a reactor where a number of gases can be supplied depending on the film needed. The fundamental principle behind the process is that a chemical reaction takes place between the source gases. The product of the reaction condenses on the substrates inside the reactor. One of the problems with CVD is the relatively high deposition temperature (600ºC), which will restrict what materials can be used. Additionally the rather slow deposition rates and hazardous byproducts formed during the processing add to the problems of using CVD. Some benefits of the process include quality films with less defects. Generally higher process temperature results in better film quality. Two variations in CVD technology are low pressure CVD which produces layers with excellent uniformity of thickness, and plasma enhanced CVD (PECVD). PECVD can take place at temperatures down to 300ºC due to the extra energy supplied to the gas molecules by the plasma.

2.1.3 Electroplating

This process is restricted to depositing electrically conductive materials (metals). A substrate, acting as a cathode, is placed in a plating bath or electrolyte solution which contains metal ions. An anode is positioned near the edge of the tank and when voltage is applied to the loop, the positively charged metal ions in the bath migrate towards the substrate. The electrons located at the cathode are neutralized causing a metal film to adhere to the cathode (substrate). When electroplating is performed without a power source, it is called electroless deposition, and requires reducing agents to supply ions. A simple representation of the electroplating process can be seen in Figure 9.

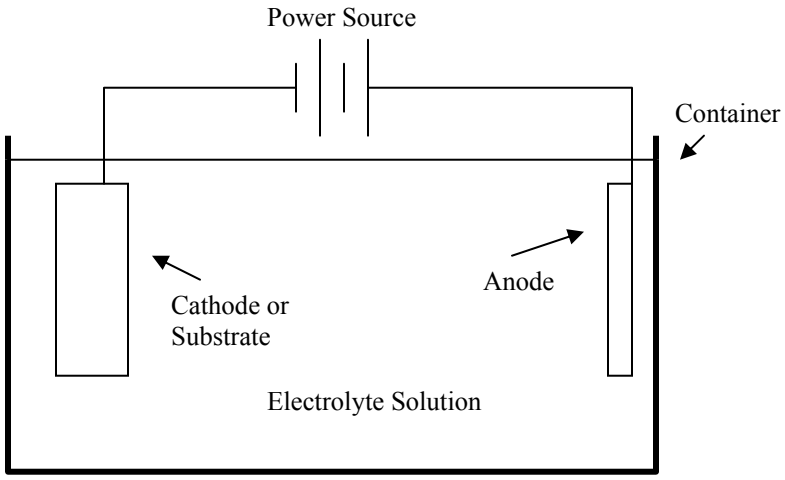

Figure 9. Schematic of an electroplating system.

Some common deposition processes have been described and due to the deposition parameters chosen, mechanical properties will vary. Bulk material properties will not always be sufficient for predicting thin film properties, and for this reason nanoindentation is used for measuring thin film mechanical properties.

2.2 Modulus and hardness measurements by nanoindentation

The most popular method for testing mechanical properties of thin films on the sub-micron scale is nanoindentation. Elastic modulus and the hardness are the two mechanical properties that can be measured by nanoindentation. The Hysitron TriboIndenter® was used for adhesion and mechanical properties testing in this thesis. It has nanometer depth resolution due to its highly sensitive three plate capacitive transducer and atomic force microscope-like (AFM) imaging capabilities (Figure 10).

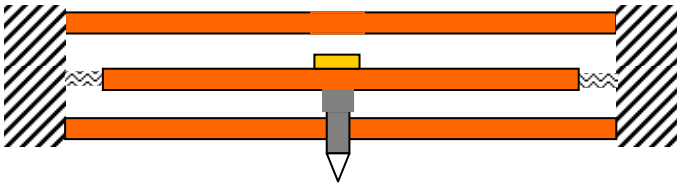

Figure 10. Hysitron three plate capacitor transducer.

There are diamond tips available of various shapes that can be used for different testing conditions. While the diamond tip is indenting the sample of interest, the load and displacement are continuously recorded in real time. The upper unloading portion of the indentation curve can be used to determine the film stiffness $S = dP/dh$, where P is described by the power relation given by Oliver and Pharr [25]:

$$P = A(\delta - \delta_{pl})^m \qquad (18),$$

where A and m are fitting parameters, P and δ are the load and displacement taken from the top 65% of the unloading curve (Figure 11).

After the film stiffness is known the reduced elastic modulus can be calculated as [25]:

$$E_r = \frac{\sqrt{\pi}}{2}\frac{S}{A_c} \quad (19),$$

where A_c is the contact area. It has been observed that the contact area remains constant as the indenter is unloaded even though there is a slight depth recovery. Since the indenter itself has finite elastic properties, its deformation contributes to the measured displacement. The reduced modulus E_r can be expressed in relation to the film and indenter modulus and Poisson ratio as [25]:

$$\frac{1}{E_r} = \frac{1-\nu^2}{E} + \frac{1-\nu_{ind}^2}{E_{ind}} \quad (20),$$

where E and ν are film elastic modulus and Poisson's ratio and E_{ind} and ν_{ind} are the elastic modulus and Poisson's ratios of the indenter.

Hardness H, is a material's resistance to plastic deformation and is defined as:

$$H = \frac{P_{max}}{A} \quad (21),$$

where A is the projected area of contact (a function of the indentation depth) at the maximum load P_{max}. Since both the elastic modulus and hardness calculations are based on the contact area produced during indentation, tip area calibration is very important. Tip area calibration is achieved by making a series of indents into a sample with known mechanical properties such as fused quartz or single crystal aluminum. Since the elastic modulus of the sample is known, it can then be used to back calculate the tip area function.

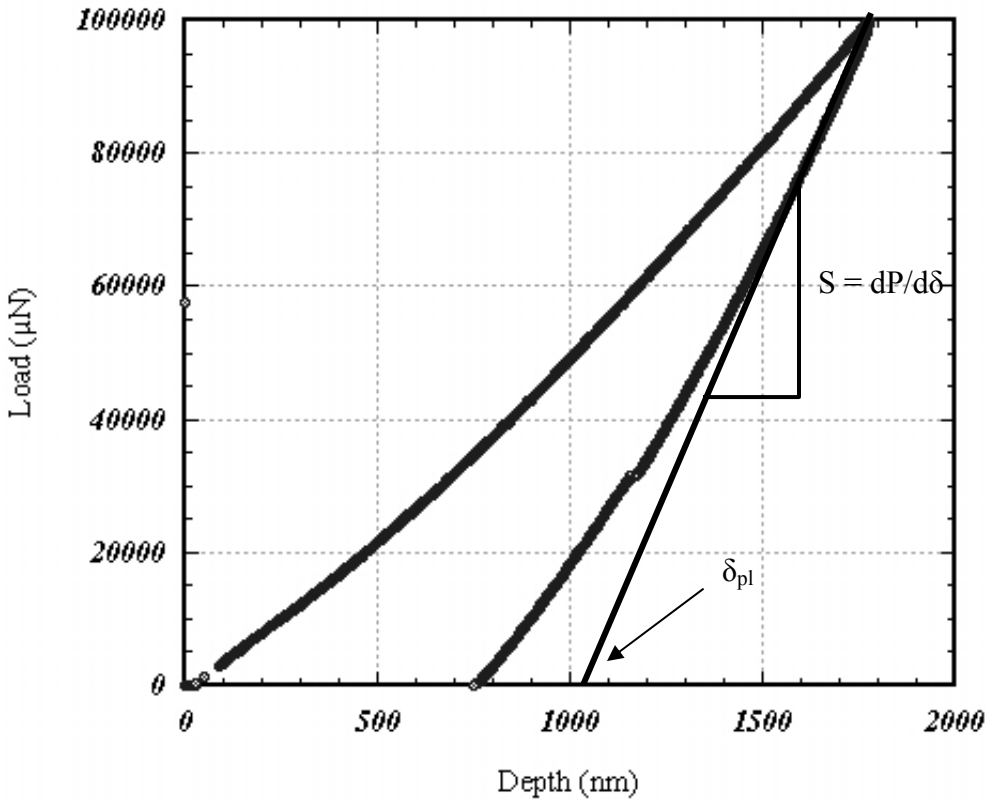

Figure 11. Load-displacement curve used to calculate the film modulus and hardness.

Some precautions should be taken while trying to measure mechanical properties by nanoindentation. Indents should not be made too deep into the thin film because effects of the substrate may be noticed [26]. In the attempt to compensate for substrate effects on the thin film elastic modulus and hardness, shallow indents are made relative to the film thickness. At the same time, if indents are not deep enough, elastic modulus and hardness measurements will be inaccurate. This inaccuracy is due to surface roughness, possible oxidation effects and errors in tip geometry due to machining limitations and blunting of the tip [27]. Topographical scans of the indent should also be made on very ductile films to ensure that no pile up occurred around the rim of the indent which could

also produce errors in contact area. A topographical image of an indent using the scanning capabilities of the Hysitron Trioboindenter® can be seen in Figure 12.

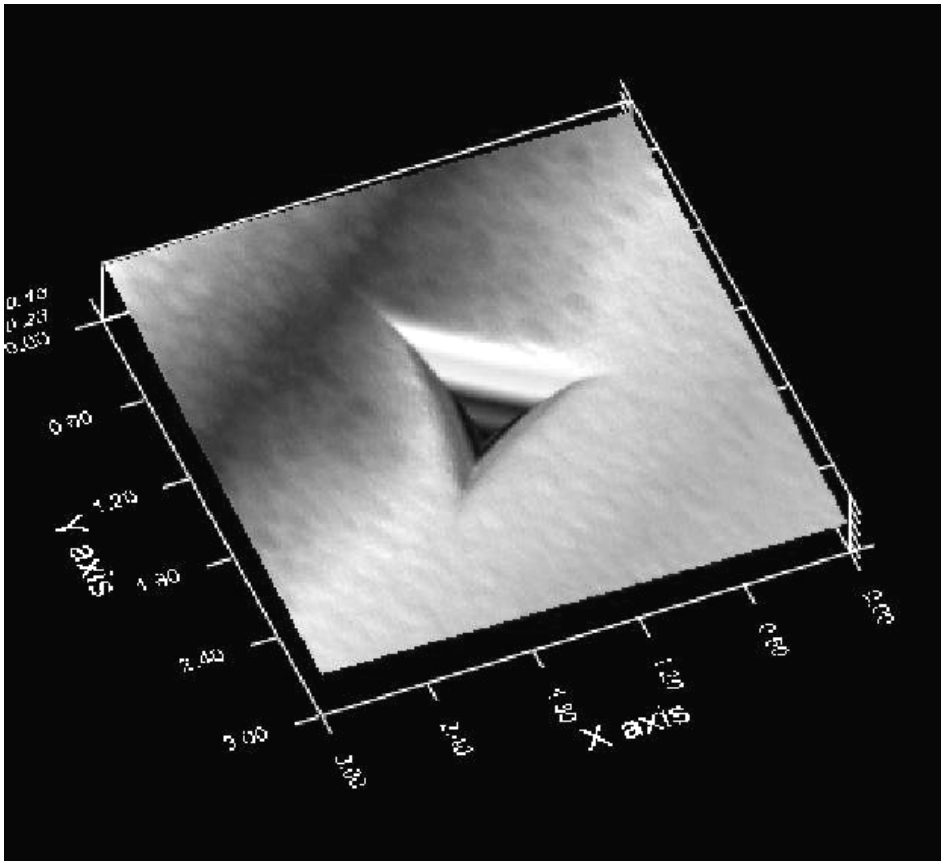

Figure 12. Topographic scan of an indent made in single crystal Al.

The same nanoindenter tool was also used for thin film adhesion measurements. Not only can the Hysitron Triboindenter make nanoscale indents for elastic modulus and hardness measurements, but it can also produce scratches to find friction coefficients and study film wear resistance.

2.3 Thin film adhesion tests

There are many different tests currently being used for measuring thin film adhesion. Some tests require very little sample preparation, while others are more time consuming and require thin film patterning using photolithographic techniques [28, 29]. One of the earliest attempts to measure adhesion was made by Strong in 1935 [30], where scotch tape was used to get qualitative results for adhesion. The scotch tape method was obviously inadequate and would not work if the adhesion of the thin film was greater than the stickiness of the tape. No matter what type of thin film adhesion test is being employed, all tests require some type of external driving force and/or internal stored energy to achieve thin film delamination. The most common types of thin film adhesion tests that are currently being used and will be described are scratch, four-point bend and indentation tests.

2.3.1 Scratch test

The scratch test is a combination of two operations: a vertical indentation motion and a horizontal dragging motion. While the tip is being dragged horizontally on the surface of the thin film, an increasing load in the vertical direction is applied until a critical load is reached and the thin film detaches from the substrate. The critical load is then measured and used to calculate the practical work of adhesion of the film to the substrate [31]:

$$P_{cr} = \frac{\pi r^2}{2}\left(\frac{2EW_{A,P}}{h}\right)^{\frac{1}{2}} \qquad (22),$$

where r is the contact radius, E is the elastic modulus of the film, $W_{A,P}$ is the practical work of adhesion and h is the film thickness. Equation 22 only applies when the normal force applied to the film surface drives its delamination, and does not account for residual stress in the thin film.

A model was later developed to account for both the residual stresses in the film and the elastic stress distribution from the scratch for estimating the strain energy release rate G_0. The first term in the following equation was developed by Hutchinson and Suo [13] and accounts for intrinsic stresses. The second term is the elastic strain energy per unit area stored in the film from the scratch test elastic stress distribution [32]:

$$G_o = \left(\frac{(1-\upsilon^2)\sigma_r^2 h}{2E} \right) + \sum \left(\frac{(1-\upsilon^2)\bar{\tau}_{ij}^2 h}{2\mu} + \frac{(1-\upsilon^2)\bar{\sigma}_{ij}^2 h}{2E} \right) \quad (23),$$

where σ_r is the residual stress, τ_{ij} and σ_{ij} are the average elastic shear and normal stresses in the delaminated film and μ is the film shear modulus.

It has been observed that most spalls created around the scratch track are symmetric, and in those cases the strain energy release rate can be estimated using a circular blister analysis [13, 33, 34 below]:

$$G = \frac{(1-\upsilon)h\sigma^2}{E} c \left[\left(1 - \frac{\sigma_B}{\sigma} \right)^2 \right] \quad (24),$$

where $c = [1 + 0.902(1 - \nu)]^{-1}$ [13] and σ_B is the Euler buckling stress.

2.3.2 Four-point bend test

The four-point bend test is becoming a popular type of adhesion test and is pictured in Figure 13. The test comprises of a central notch that runs through the

thickness of the top layer and a symmetrical precrack is induced along the interface upon loading. The notch in the top layer is usually made using a high speed dicing saw [20, 35] and crack propagation will occur when a critical load is reached.

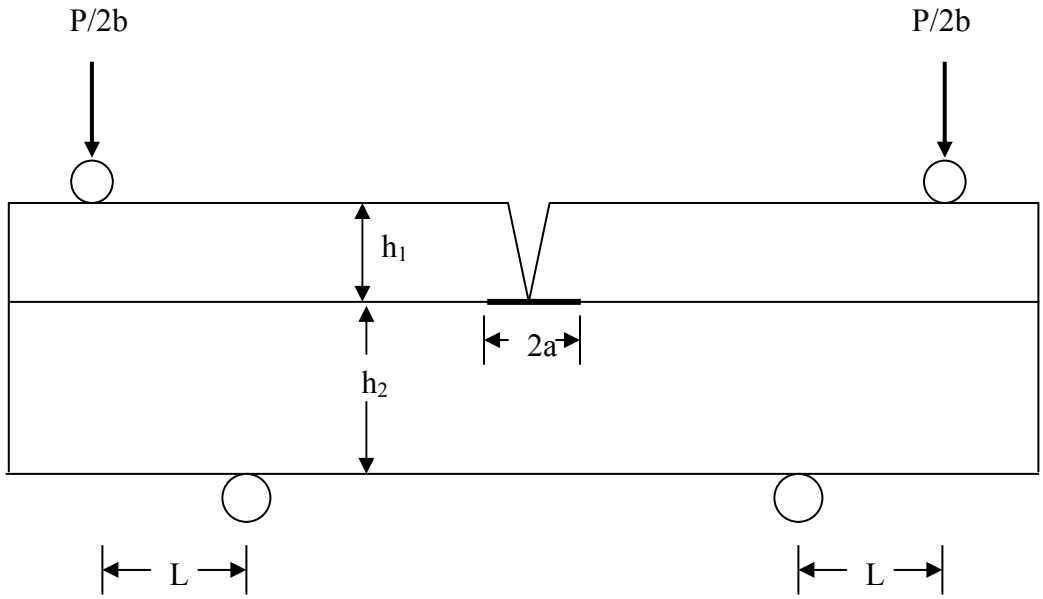

Figure 13. Schematic of a four-point bend test.

For the crack located between the inner loading lines there is a constant moment condition and the strain energy release rate should exhibit steady-state characteristics. The steady state value G_{ss} is deduced analytically by recognizing that it is the difference in strain energies in the uncracked and cracked beams [36]:

$$G_{ss} = \frac{M^2\left(1-\upsilon_2^2\right)}{2E_2}\left(\frac{1}{I_2}-\frac{\lambda}{I_c}\right) \quad (25),$$

where

$$\lambda = \frac{E_2\left(1-\nu_1^2\right)}{E_1\left(1-\nu_2^2\right)} \quad (26),$$

$$I_c = \frac{h_1^3}{12} + \frac{\lambda h_2^3}{12} + \frac{\lambda h_1 h_2 (h_1 + h_2)^2}{4(h_1 + \lambda h_2)} \quad (27),$$

$$I_2 = \frac{h_2^3}{12} \quad (28),$$

where the subscript *c* refers to the composite beam. The moment per unit width is $M = Pl/2b$, with P being the total load and l is the spacing between inner and outer load lines. Trends in G_{ss} with relative dimensions h_1/h_2 and relative modulus E_2/E_1 are depicted in Figure 14. With an increase in upper beam thickness there is an increase in G_{ss}, and an increase in the modulus of the lower layer results in G_{ss} decrease.

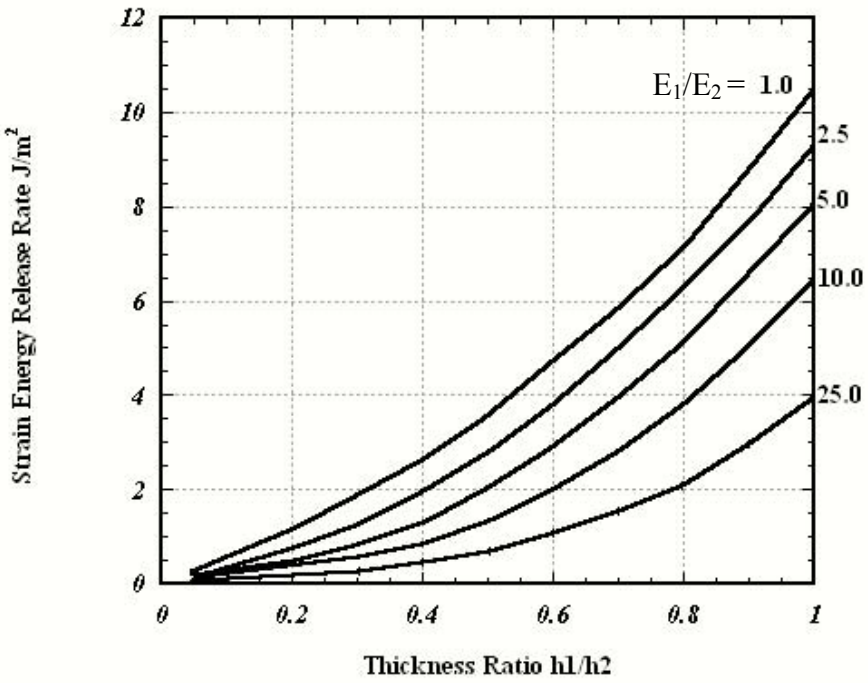

Figure 14. Trend in steady state strain energy release rates with the film thickness and modulus ratios [36].

The four-point bend technique is a very effective test for measuring global adhesion values and has the ability for the user to control the applied strain energy release

rate. Currently it is successfully being used to measure the effects of environmentally assisted fracture on crack propagation rates [20]. The four-point bend test has its benefits and is becoming a widely used adhesion test for thin films. It was not, however, used for the adhesion measurements taken in this thesis, the superlayer indentation test was used instead. When using nanoindentation for adhesion measurements, all derivations and equations used are based on a one-dimensional buckling analysis. Before the indentation test can be described, a one-dimensional buckling analysis must be outlined.

2.3.3 One-dimensional buckling analysis

Hutchinson and Suo have made the following assumption and have provided solutions for the residual stress and the energy for interfacial fracture for a one-dimensional or straight wall buckle:

1) The film and the substrate are elastic isotropic solids;
2) The unbuckled film is subject to uniform, equi-biaxial compressive in-plane stress, $\sigma_{xx} = \sigma_{yy} = -\sigma_r$ (Figure 15 (a));
3) The film thickness *h* is much less than the buckling width *2b* (Figure 4);
4) The substrate is infinitely thick.

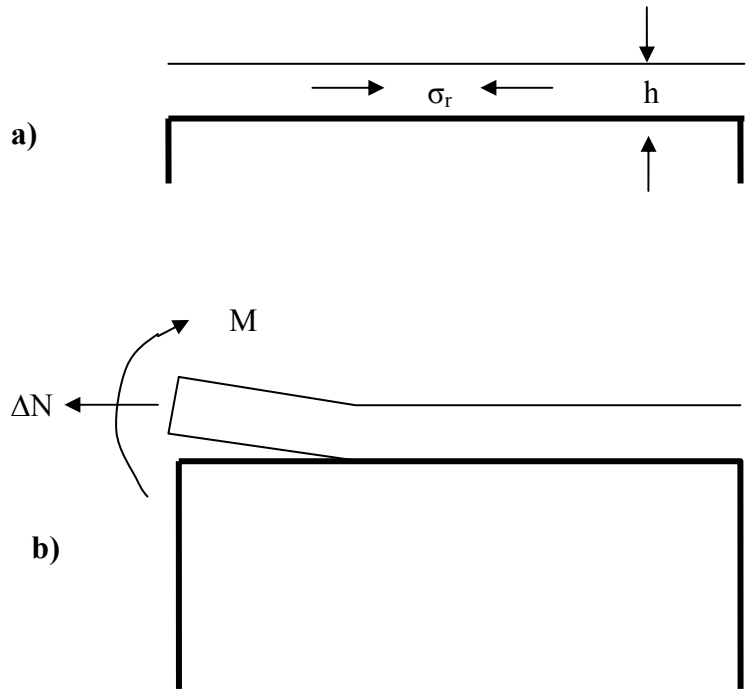

Figure 15. One-dimensional buckle schematic: a) Residually stressed thin film, b) Forces applied to a buckled thin film.

The buckle is modeled as a wide, clamped Euler column of length 2b seen in Figure 4. For a blister to form under these conditions without any externally applied forces, the compressive residual stress σ_r, must exceed the buckling stress σ_B [13]:

$$\sigma_B = \frac{\pi^2}{12}\frac{E}{(1-\upsilon^2)}\left(\frac{h}{b}\right)^2 \qquad (29),$$

where E is the film's elastic modulus, v is the Poisson's ratio of the film, h is the film thickness and b is the blister half-width. The residual stress can then be determined from the blister height and buckling stress [13]:

$$\sigma_r = \sigma_B\left[\frac{3}{4}\left(\frac{\delta}{h}\right)^2 + 1\right] \qquad (30),$$

where δ is the blister height.

For a large residual to buckling stress ratio, the strain energy release rate asymptotically approaches [13]:

$$G_0 = \frac{(1-\upsilon^2)h\sigma_r{}^2}{2E} \quad (31),$$

where G_0 is the strain energy per unit area stored in the film.

When the thin film is under high compressive stress, it can be relieved by buckling and the strain energy release rate is given by [13]:

$$G = \frac{(1-\upsilon^2)h}{2E}(\sigma_r - \sigma_B)(\sigma_r + 3\sigma_B) \quad (32),$$

The strain energy release rate defined in Equation 31 is equal to the interfacial fracture toughness of the thin film when delamination occurs.

2.3.4 Indentation test

Nanoindentation is a very successful way for measuring the elastic modulus and hardness of thin films [25], but it can also be used to measure thin film adhesion. Delamination and crack growth are induced with the combination of indentation stresses and residual stresses present in the thin film. Marshall and Evans treated the section of film above the delaminating crack induced by indentation as a rigidly clamped disc shown in Figure 16 [34].

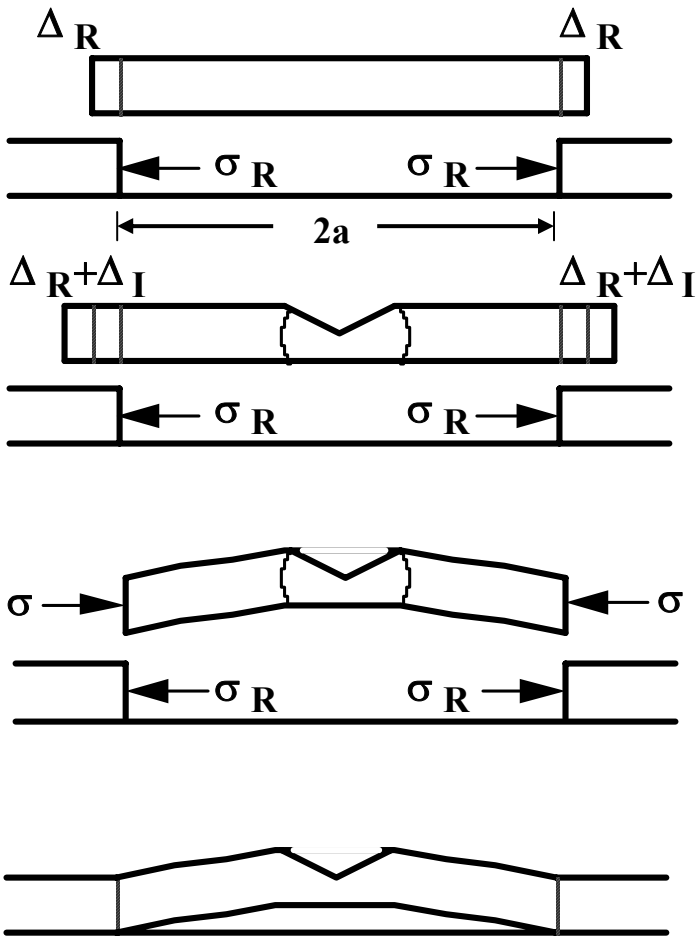

Figure 16. Hypothetical operations used to calculate the strain energy associated with an indentation-induced delamination in a stressed film.

In the first step of Figure 16 a delaminated section is hypothetically taken out to show the effects of a compressive residual stress, if the section was going to be placed back into the sample, the section would have to be recompressed with an edge stress σ_r. The work done would be:

$$U_p = \left(\pi h a^2\right)\sigma_r \varepsilon_r \qquad (33),$$

where $\varepsilon_r = \Delta_R/a$ and $2a$ is the crack length. This is equivalent to the residual strain energy stored within the delaminated section before removal. The total energy of the system, U_R

= $U_S + U_p$, is independent of crack length for an unbuckled plate. Therefore, the strain energy in the remainder of the film, $U_S = U_R - U_p$, must depend on the delamination radius, where U_R can now be treated as a constant.

In the second step, the indentation is made and it creates a plastic zone of deformation leaving a permanent impression of volume V_I. It is assumed that volume is conserved and results in radial displacements at the crack tip. It is modeled as an internally pressurized cylinder inducing a radial expansion Δ_I at the edges equal to:

$$\Delta_I = \frac{V_I}{2\pi ha} \tag{34},$$

where the indentation strain is defined as $\varepsilon_I = \Delta_I/a$ and the stress required to recompress the section Δ_I is:

$$\sigma_I = \varepsilon_I \frac{E}{(1-\nu)} = \frac{V_I E}{2\pi ha^2(1-\nu)} \tag{35}.$$

The internally pressurized cylinder has a radius-dependent elastic strain energy distribution with a total work done of:

$$U_E = -\sigma_I \varepsilon_I \left[\frac{\pi ha^2(1-\nu)}{2}\right] \tag{36}.$$

In the third step the expanded section is recompressed by a combination of the residual and indentation stress, and the strain energy induced is:

$$U_{RI} = \pi ha^2 \left[(\sigma_I + \sigma_R)(\varepsilon_I + \varepsilon_R) + (\alpha - 1)(\sigma_I + \sigma_R - \sigma_B)(\varepsilon_I + \varepsilon_R - \varepsilon_B)\right] \tag{37},$$

where α represents the slope of the buckling load versus the edge displacement upon buckling:

$$\alpha = 1 - \frac{1}{1 + 0.902\left(1 - v_f\right)} \tag{38}.$$

For the case of non-buckling fracture, when α = 1, delamination is only driven by the indentation stress and the residual stress does not come into play. This can be seen in the following strain energy release rate Equation 38.

In step four there is reinsertion and the total strain energy is the sum of the strain energies just described. The sum of the strain energies can be differentiated with respect to the crack area *A* in order to find the strain energy release rate *G* [34]:

$$G = -\frac{d}{dA}\left(U_S + U_E + U_{RI}\right), \text{ or}$$

$$G = \frac{h\sigma_I^2\left(1 - v_f{}^2\right)}{2E_f} + \left(1 - \alpha\right)\frac{h\sigma_R^2\left(1 - v_f\right)}{E_f} - \left(1 - \alpha\right)\frac{h\left(\sigma_I - \sigma_B\right)^2\left(1 - v_f\right)}{E_f} \tag{39}.$$

Two problems likely to be encountered in a single layer indentation test are pile-up of the thin film around the indenter tip and penetration to depths greater than the film thickness. If the indent is made too deeply, deformation and cracking of the substrate may occur and would reduce the validity of the test. Both problems can be controlled using the superlayer indentation technique, which consists of depositing a hard superlayer on top of the film of interest. The superlayer can be deposited by means of relatively low temperature physical vapor technique such as sputtering, where the temperature is not high enough to alter the microstructure or interface of the original film. The superlayer can be tailored to optimize conditions for film thickness and residual stress, which allows for greater driving force for the same penetration depth to film thickness ratio. One condition that must be met for the superlayer indentation method to work is that the

superlayer must adhere to the film more strongly than the film adheres to the substrate. If this condition is not met, the measurement obtained for adhesion will be for the superlayer to film and not the adhesion of the film of interest to the substrate.

Kriese and Gerberich have combined the idea of a superlayer test with the Marshall and Evans findings by applying the laminate theory in order to calculate the strain energy release rate for a multilayer sample [37]. For many cases the superlayer is much thicker than the underlayer and the laminate theory does not need to be applied, as the test can be treated the same as the single layer test defined by Marshall and Evans.

All adhesion measurements in this thesis were performed using the superlayer indentation test. The only two measurements required to calculate the strain energy release rate are the blister radius and inelastic indentation depth. Blister radius is found by using an optical microscope (Figure 17) with a micron ruler superimposed on the lens in the eye piece. A maximum magnification of 200X was used, as an increase in magnification decreases the users' ability to see height changes in the film. At 200X magnification, the radii measurements could be taken to approximately ± 1 μm accuracy. The plastic indentation depth δ_{pl} can be found using the Oliver-Pharr method from the load-displacement curve [25] (Figure 18).

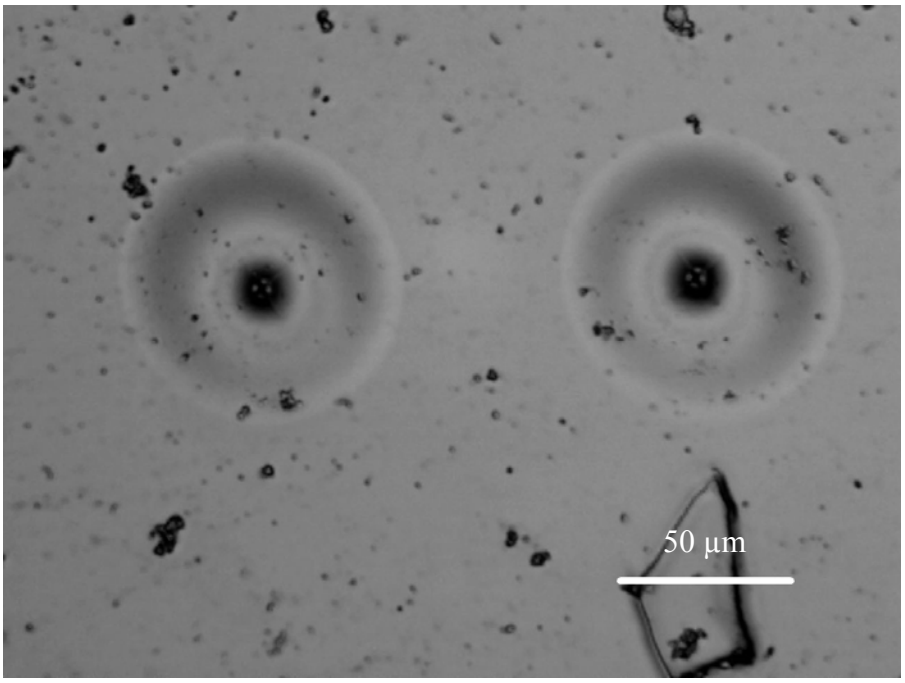

Figure 17. Delamination blister produced in the superlayer indentation test.

The delamination blisters and load-displacement curve seen in Figure 17 and Figure 18 respectively were produced using the Hysitron Triboindenter® with the multirange transducer. The same system is used for both mechanical properties testing and adhesion measurements. Two different transducers are available depending on the maximum load needed. There is almost no sample preparation required for the use of the nanoindenter when testing thin film mechanical properties and adhesion. The multirange transducer and stage layout of the nanoindenter are pictured in Figure 19.

The samples are first fixed to steel backings so they can be secured on the magnetic stage. The user then controls the movement of the stage in the x and y directions to choose a location for indentation. After the user focuses the objective lens on the sample of interest, indent settings are specified. The stage will position itself so that the transducer is now above the location where the objective lens had previously

focused. The transducer and objective lens then move in the z direction upon indentation. After the indent has been completed the transducer and objective lens are raised. The stage is then positioned back to the original location where the objective lens was focused.

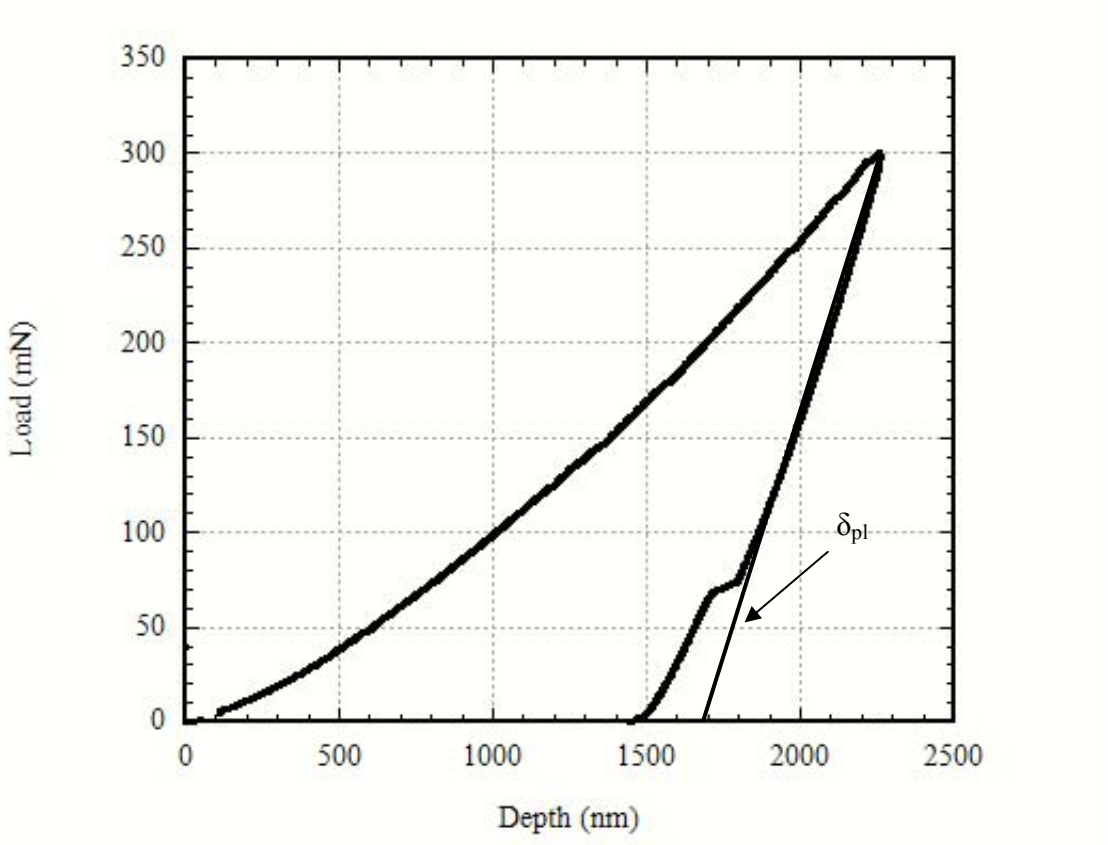

Figure 18. Load-displacement curve for plastic indentation depth determination.

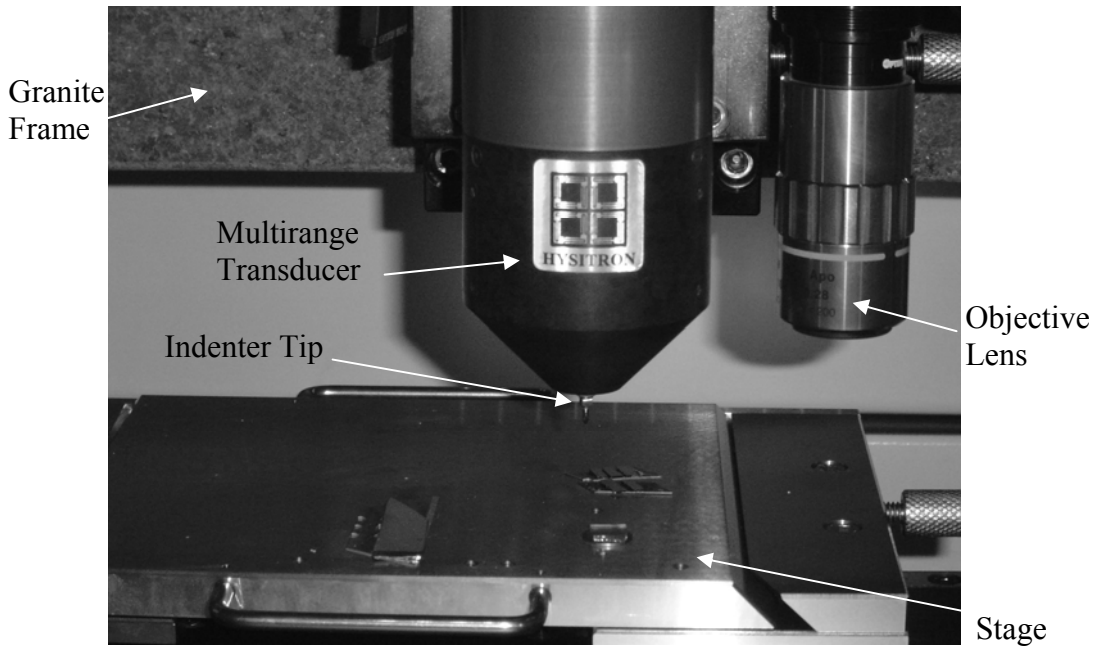

Figure 19. Nanoindenter with a multirange transducer.

2.4 Residual stresses

If the proper conditions are not met during deposition of thin films, high residual stresses may be present, leading to film failure. Residual stresses can be partially relieved through plastic deformation, cracking, or delamination. Residual stresses in tension usually lead to cracking and interfacial delamination, while residual stresses in compression typically lead to film buckling and delamination from the substrate [38]. In the superlayer indentation test the thin film residual stresses provide additional energy helping to propagate a crack along at the film/substrate interface. The use of residual stresses allows for lower externally applied loads needed to induce delamination in the superlayer indentation test.

When using PVD methods film thickness can sometimes vary up to as much as 10% on a 4 in. diameter wafer [39]. For copper thin films residual stress increases with

increasing film thickness, where in molybdenum thin films residual stress decreases with increasing film thickness [39, 40]. Figure 21 shows that there can be up to 50% variation in residual stress in a 6 in. diameter wafer. Laser deflection and optical lever cantilever beam techniques were used to get average residual stresses across the entire wafer [38].

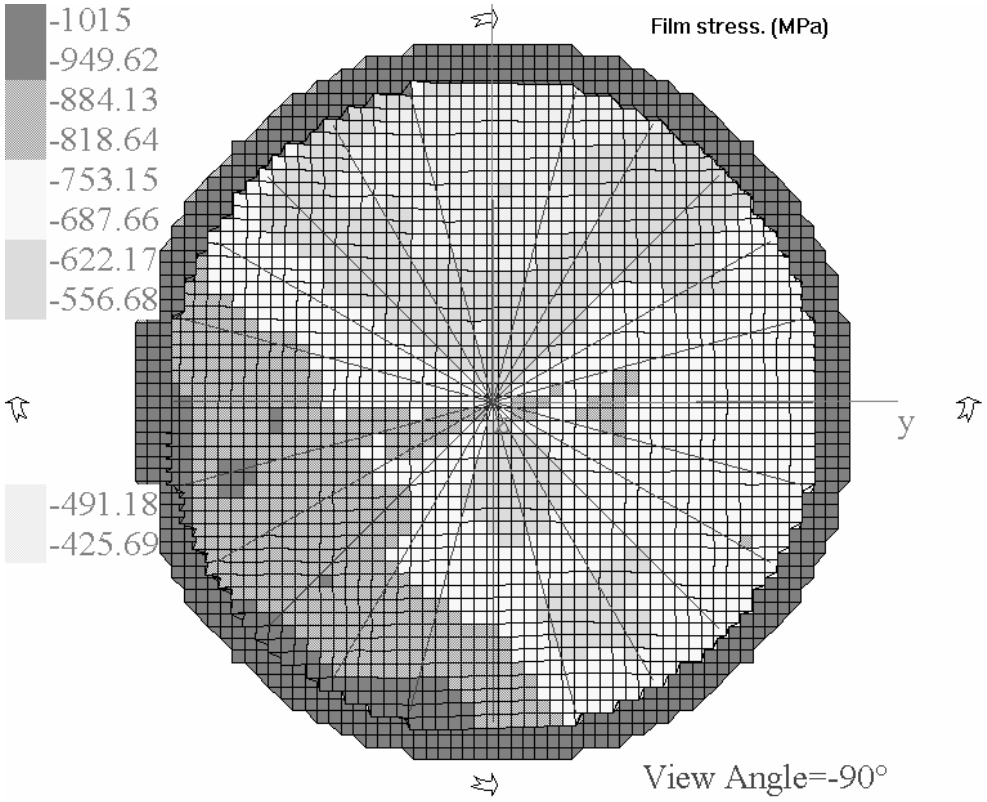

Figure 20. Residual stress map of a 1 µm W film on a 6" Si wafer [38].

2.4.1 Stoney's equation

Since the mid 1800's it was well known that metallic films deposited by electroplating would peel off if deposited to any considerable thickness. It was concluded that the metals deposited where under tension. The average residual biaxial stresses in the films can be calculated by using the Stoney equation [41]:

$$\sigma_r = \frac{E_s}{6(1-\nu_s)}\frac{h_s^2}{h_f}\left(\frac{1}{R_2}-\frac{1}{R_1}\right) \quad (40),$$

where E_s is the elastic modulus of the substrate, ν_s is the Poisson's ratio of the substrate, h_s is the substrate thickness, h_f is the film thickness, R_1 is the radius of curvature of the substrate before deposition and R_2 is the radius of curvature of the substrate after deposition. The Young's modulus of the film is not required to evaluate the stresses in the film with this method because the film thickness is considered insignificant compared to the substrate thickness.

2.4.2 X-ray diffraction for stress determination

In X-ray diffraction the strain in the crystal lattice is measured and the residual stress producing the strain is then calculated, assuming a linear elastic distortion of the crystal lattice. To determine the stress, the stain in the crystal lattice must be measured for at least two precisely known orientations relative to the sample surface (Figure 21). Therefore, X-ray diffraction for residual stress measurement is applicable to materials that are crystalline and isotropic.

The $\sin^2\Psi$ technique is a successful method used for finding residual stress by means of X-ray diffraction, where residual stress is defined as [42]:

$$\sigma_\phi = \left(\frac{E_f}{1+\nu_f}\right)\frac{1}{d_0}\left(\frac{\partial d_{\phi\Psi}}{\partial \sin^2\Psi}\right) \quad (41),$$

where d_0 is the unstrained lattice spacing for the crystal structure of concern and $\partial d_{\varphi\psi}/\partial sin^2\Psi$ can be found by plotting the lattice spacing found at the varying angles of Ψ, against the values of $\sin^2\Psi$ seen in Figure 22. Stress in the z-direction is assumed to be

zero, and if the slope of the plot seen in Figure 22 is linear, biaxial stress can be assumed [42].

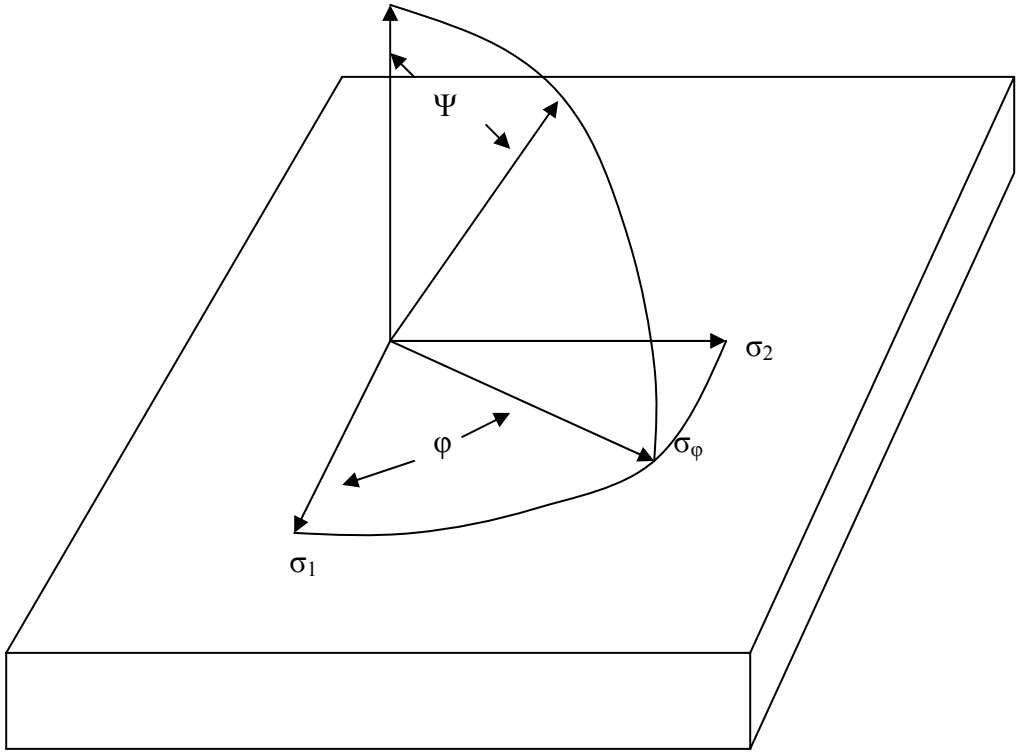

Figure 21. Sin^{2}Ψ technique setup.

Residual stress measurements were taken on a tungsten film using both the Stoney equation and the sin^{2}Ψ technique. An average biaxial compressive residual stress of 1 GPa was calculated with the Stoney equation and a locally measured value of 1.33 GPa was determined using the sin^{2}Ψ technique. These values correspond to the changes in residual stress that can be seen across a wafer by up to 50%, similar to the results shown in Figure 20. For the tungsten film tested, the majority of crystallographic planes detected were in the (220) direction, which corresponds to a peak at the 2θ angle of 86.54° (Figure 23).

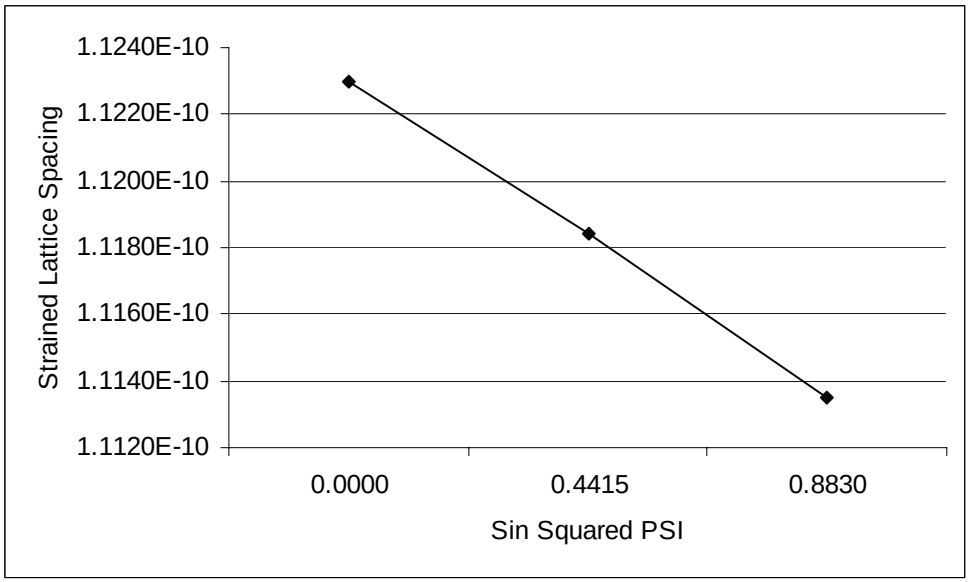

Figure 22. Strained lattice spacing vs. $\sin^2\Psi$ for a tungsten thin film.

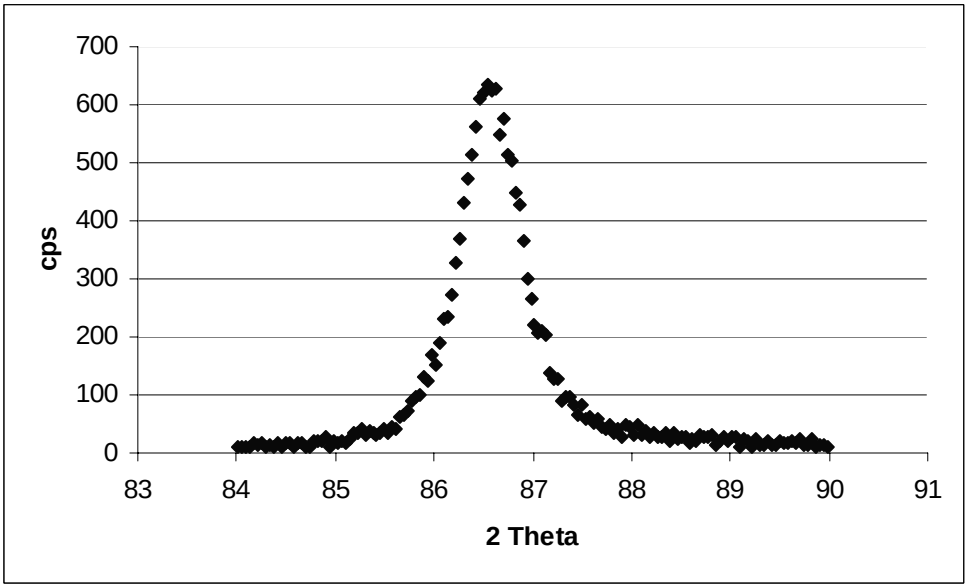

Figure 23. X-ray data for (220) tungsten film.

CHAPTER 3

ADHESION MEASUREMENTS

3.1 Sample preparation

Adhesion measurements in dry and wet environments were conducted on three different samples. One sample had a 5 nm thick diamond like carbon film (DLC), deposited by PECVD on a 3" silicon wafer with a 300 nm thick layer of SiO_2 and was supplied by Seagate. An 800 nm thick tungsten superlayer was sputter deposited on top of the DLC film (1.9 GPa compressive residual stress). Amorphous carbon films 5-10 nm thick are applied on the surface of magnetic media for protection. DLC films are being used due to their chemical inertness, high hardness and wear resistance with low friction coefficients [43, 44]. High adhesion of DCL films is required, because any delamination of the coating from the surface can damage the head and make media unreadable.

The two other samples of interest were copper films sputter deposited on a silicon substrate with a 1 μm layer of SiO_2. A 1.1 μm thick tungsten superlayer was sputter deposited on top of both copper films (320 MPa compressive residually stress). The first copper film tested was 67 nm thick, and the second was 97 nm thick. Copper adhesion has been of interest since the late 1990's when research was conducted regarding the possibilities of replacing aluminum with copper as the choice for interconnect material in microelectronics. Not only does copper have better electrical and thermal conductivity

than aluminum, copper interconnects provide higher current densities and better electromigration performance. One major disadvantage, however, of using copper films is that they have lower adhesion to Si substrates than aluminum. For this reason, it was necessary to quantify the adhesion of copper to silicon and to experiment with moisture effects that may be seen in a production environment.

3.2 Adhesion measurements in a dry environment

Once the samples are prepared, testing adhesion using the indentation method is relatively simple. One point to keep in mind when using indentation, is that when an indent is made, the strain energy release rate measured is only for a small area of the sample. To compensate for this localized effect, 4 trials of indents were made at different locations on each sample. Each trial consisted of 5 to 10 indents at varying loads, with the same load variation being used for each trial. The Hysitron Triboindenter was used for all of the adhesion measurements and all parameters and settings remained consistent for all the samples.

Indentation was performed under load control, while the total indent time was kept the same for all indents on three different samples. Every time, prior to use, calibration of the transducer was performed before the indents were made. For each trial it was important to achieve matching of load-displacement curves in order to verify that the indentation process was working properly and that the calibration had been done correctly. Load-displacement curves may vary slightly between the different trials due to variations in film thickness and residual stress. The first trial of indents performed on the 97 nm thick sample of copper is shown in Figure 24.

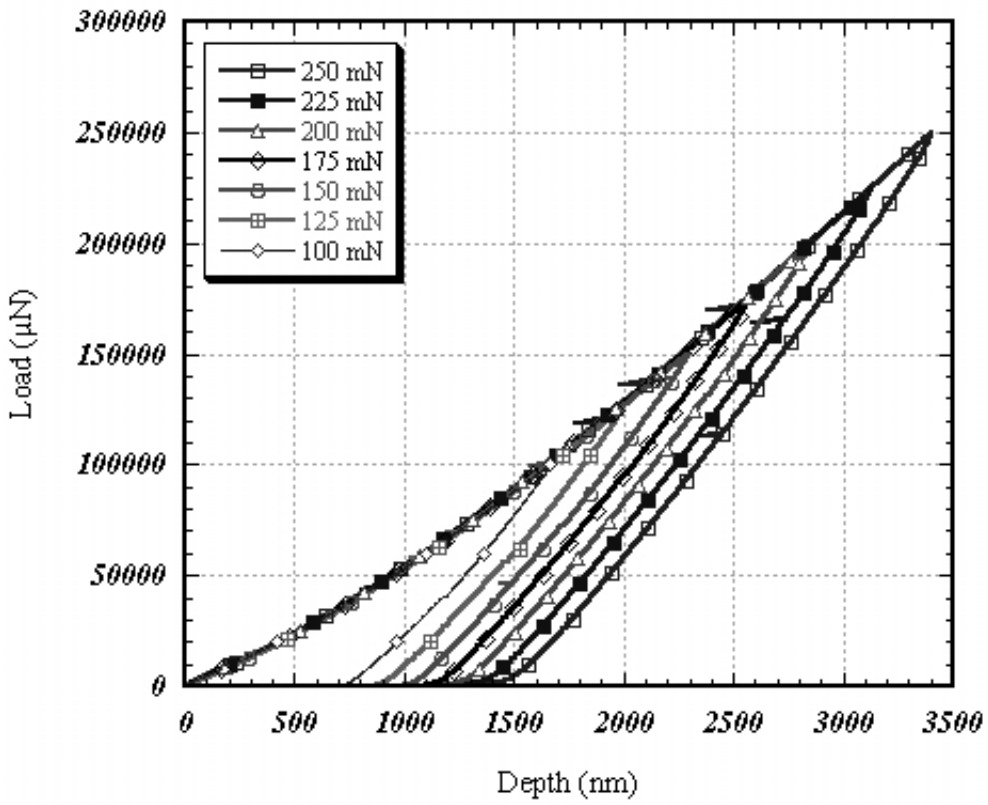

Figure 24. Load-displacement curves for a 97 nm thick copper film.

To ensure that usable measurements were taken, it was necessary to keep the maximum loads within a certain range. If the loads applied were too small, no delamination blisters appeared. If too high of a load was applied, extensive radial cracks appeared in the thin film along with substrate fracture, making adhesion calculations less accurate. The range for the maximum applied loads on the DLC film was from 200 mN to 400 mN. For the 67 nm and 97 nm thick copper films the maximum load was kept between 100 mN and 275 mN. Figure 25 shows radial cracks that appeared if too high of a load was applied. Large excursions in the load-displacement curves were noticed every time extensive radial cracking was seen in the buckled thin film (Figure 26). Further investigation of the shifts in the load-displacement curves will need to done to explain

their appearance. Besides film cracking, their presence could also be attributed to substrate fracture or buckling of the thin film upon interface debonding. It was observed that the shifts in the load-displacement curves would repeatedly appear around the same load for each sample.

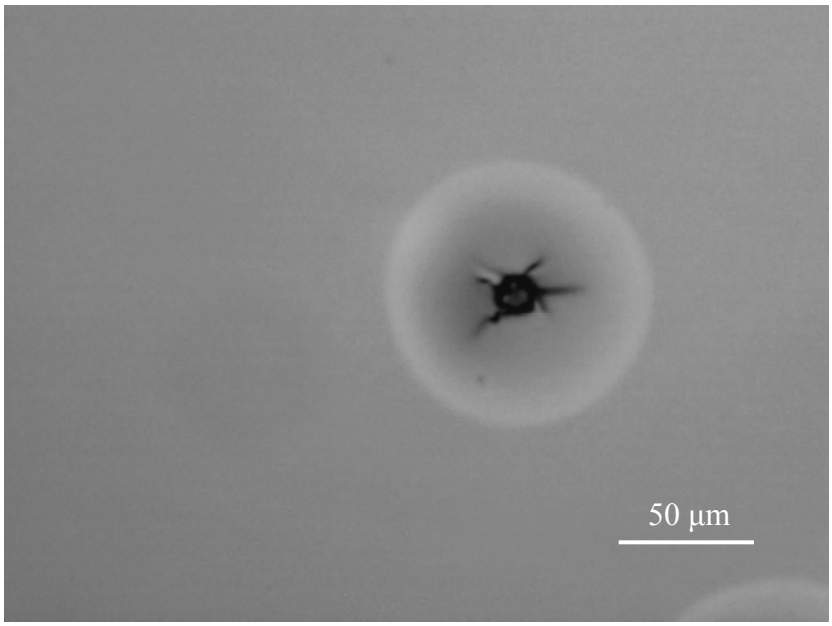

Figure 25. Radial cracks in delamination blister.

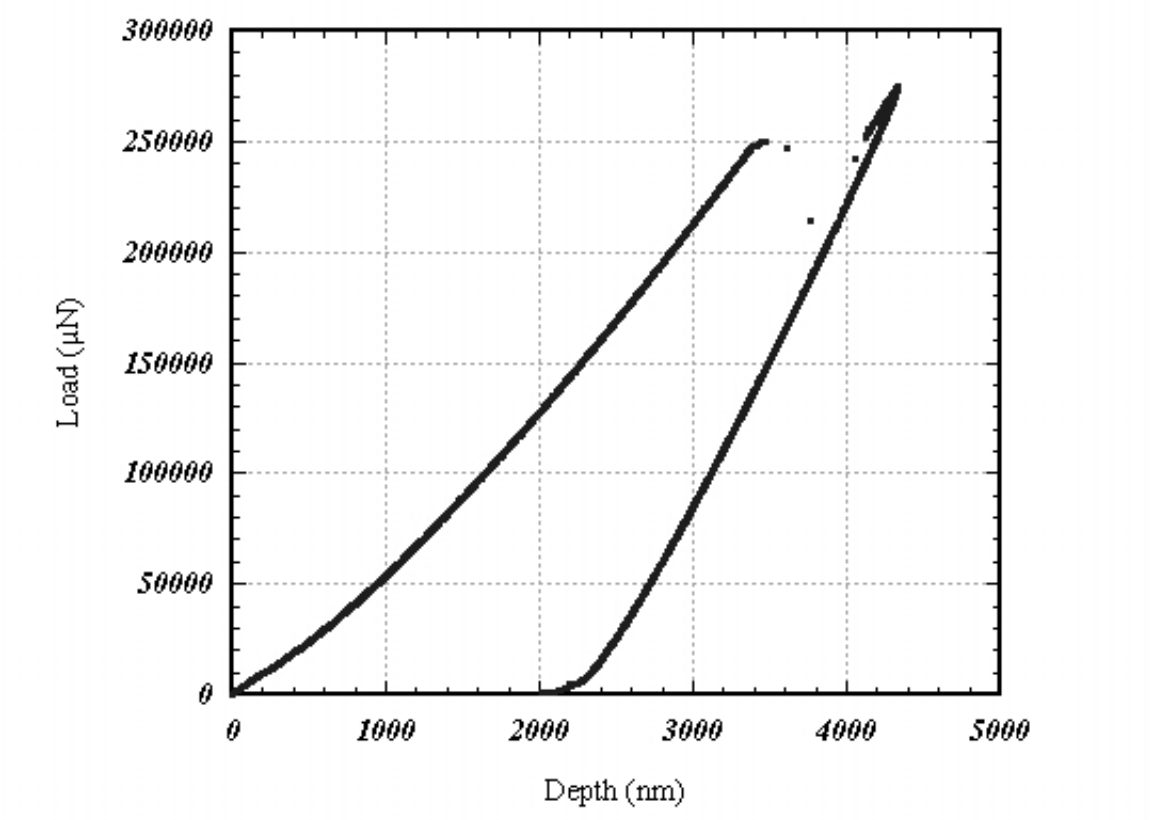

Figure 26. Shift in load-displacement curve.

The strain energy release rates have been plotted against the ratio of the delamination blister radius to the contact radius, x/a, defined in Figure 27. For smaller indents and x/a ratios, larger strain energy release rates were measured and as the indents were made to greater depths and larger x/a ratios, the strain energy release rate decreased (Figure 28 - Figure 30).

The steady state adhesion value is assumed when the strain energy release rate starts to plateau off at larger x/a ratios. This value is taken because there are two components that contribute to the elastic energy in the film that drives interfacial delamination. For smaller indents, where $x/a < 5$, there is an indentation-induced stress that drives interfacial cracking. For x/a ratios greater than 5, the residual stress in the

superlayer is the largest contributing factor for interfacial crack growth [45]. For the adhesion values reported here, the plateau in strain energy release rate occurred at x/a ratios greater than 8. A comparison of the adhesion measurements for the three different films in a dry environment are seen in Table 1, where the strain energy release rate was averaged for a delamination blister radius to crack length ratio between 9 and 12.

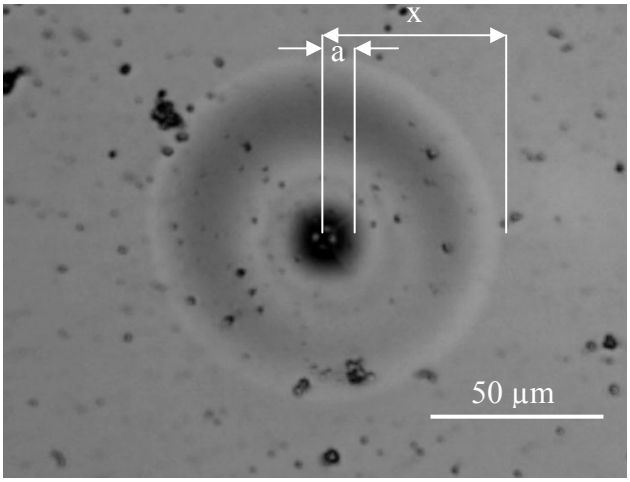

Figure 27. Definition x/a dimensions.

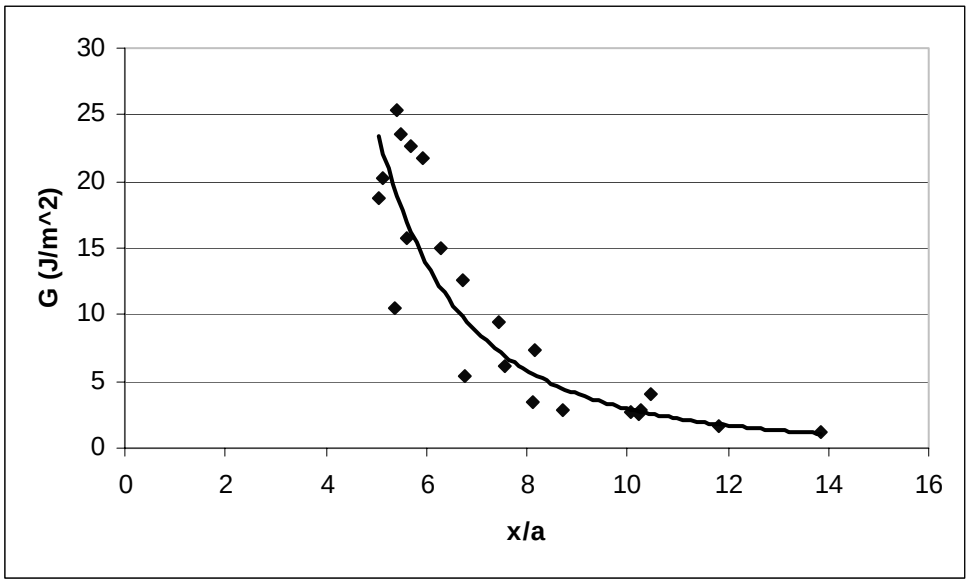

Figure 28. Strain energy release rates for the 67 nm thick copper film.

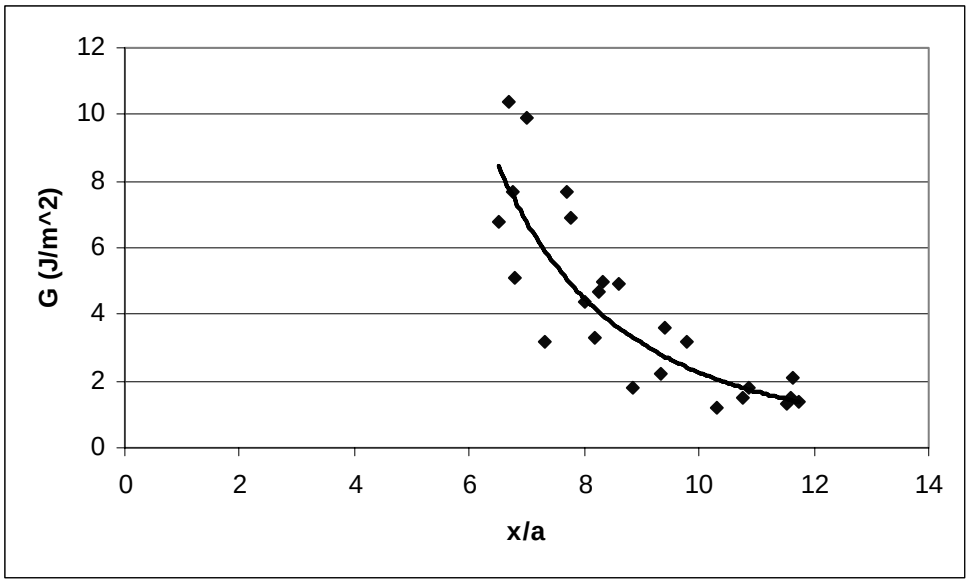

Figure 29. Strain energy release rates for the 97nm thick copper film.

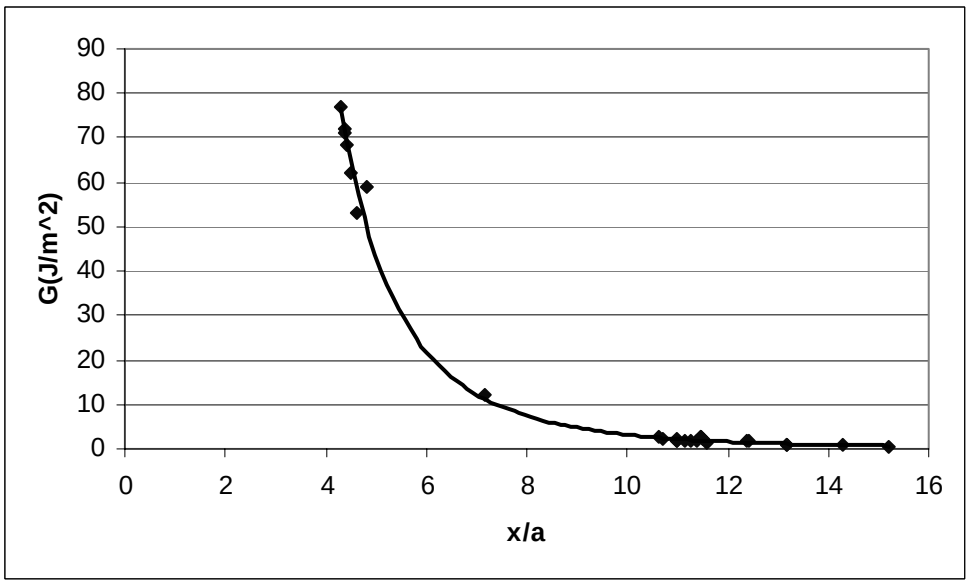

Figure 30. Strain energy release rates for the 5 nm thick DLC film.

When the strain energy release rate is plotted against the x/a ratio, all three samples exhibit a similar parabolic shape behavior. A power trendline was plotted on Figure 28 - Figure 30 using the equation $y = cx^b$ to calculate the least squares fit through the data points. All film adhesion measurements were recorded for x/a ratios of 9-12, which can be compared to the ratio of indentation depth to bi-layer film thickness. It is interesting to note the differences in depths needed to reach larger x/a ratios. Substrate fracture is likely to occur if indentations are made too deep, which may lead to inaccuracies in adhesion measurements. Further tests will need to be made to look at the effects of making deeper indents, where the indenter tip penetrates over a micron into the silicon substrate.

Table 1. Strain energy release rates in dry environment.

Sample	x/a	Depth/Thickness	G (J/m^2)
Cu 67 nm	9 - 12	1.5 - 2.4	2.74 ± 0.86
Cu 97 nm	9 - 12	0.8 - 1.8	1.98 ± 0.82
DCL 5 nm	9 - 12	2.0 - 3.5	2.09 ± 0.31

Past tests have been conducted on the same copper samples where the strain energy release rate for a 67 nm thick layer of copper was recorded to be between 0.4 and 2.0 J/m^2 and for the 97 nm thick film of copper the recorded value was between 0.1 and 0.5 J/m^2 [45]. Discrepancies in reported strain energy release rates and the present study are thought to be due to a 7-year period of time between the copper film adhesion tests. Over such a long time copper diffusion into the SiO_2/Si layers could be causing higher

recorded adhesion values. Due to the localized nature of the indentation test, various areas of the initial wafer should be tested to get a more accurate average film adhesion.

Whether or not the exact same values were reported, the trend is the same for the two different studies. Film adhesion was measured to be lower for the 97 nm thick copper film than for the 67 nm thick copper film. Table 2 reports copper film adhesion from the past tests and also compares copper adhesion to aluminum and titanium underlayers on a silicon substrate. Different types of underlayers or barrier layers such as titanium, tantalum and tungsten have been shown to increase film adhesion to the silicon substrate. Underlayers have helped solve the problem of copper diffusion into the substrate and interlayer dielectric (ILD).

Table 2. Adhesion of thin films in dry environment.

Sample	Thickness (nm)	G (J/m^2)	Reference
W/Cu/SiO_2/Si	40 - 4000	0.2 – 2	[1, 45-49]
W/Cu/Ti/ SiO_2/Si	40 - 4000	3.63	[1, 45]
W/Al/ SiO_2/Si	40 - 3200	4 – 100	[40]

3.3 Effects of indenter tip geometry on adhesion measurements

A Berkovich tip was originally used to measure the 5 nm thick DLC film adhesion and then measurements were repeated with a 1 μm radius conical tip. The results using the two different tips were then compared. Film adhesion was measured to be 4.3 ± 0.2 J/m^2 with the Berkovich tip, compared to 2.09 ± 0.31 J/m^2 with the conical tip. Higher values with the Berkovich tip were initially thought to be caused by using the

theoretical tip geometry when calculating the volume displaced by the indenter. The theoretical tip geometry does not account for a slightly blunted tip which has a tip radius between 100 – 200 nm. After examining impressions left by the Berkovich tip, neglecting the tip radius was longer thought to be the only cause of difference between the adhesion measurements. The Berkovich tip that was used had an extended shaft so that it could be used in fluids. If the tip makes penetration perpendicular to the film surface a perfectly equilateral triangle would be expected as a result.

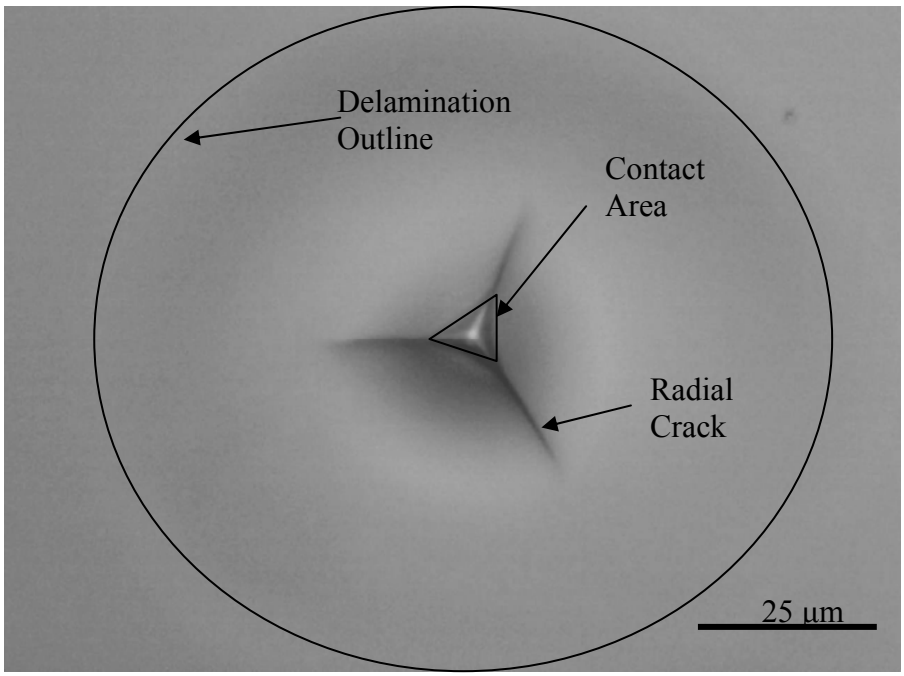

Figure 31. Delamination induced by a Berkovich tip.

Figure 31 shows the tip impression and radial cracks left by the fluid cell Berkovich tip. It is observed that the edge impression and radial crack on the lower right hand corner are slightly longer than the other two creases and radial cracks. This means that the Berkovich tip did not penetrate the film perpendicular to its surface. The slight offset of the tip would further add to the inaccuracies when calculating the displaced

volume. The conical tip was chosen for its geometry, as the slight offsets of the fluid cell shaft were less of a factor when calculating the displaced volume. Therefore, the 1 μm radius conical tip was used for all further adhesion measurements.

Blister symmetry is another important factor in analyzing delaminations for adhesion measurements. Indents made with the conical tip consistently resulted in circular blisters. Indents made with the Berkovich tip were often observed to be asymmetrical in shape (Figure 32). The main reason for the asymmetrical blister shape with the Berkovich tip could be attributed to the same reason for errors when calculating the strain energy release rates. If the tip did not come down perpendicular to the film surface it would create a small snowplow effect, resulting in an unequal force distribution.

At higher maximum applied loads with the Berkovich tip, circular blister delaminations are observed. Even when perfectly circular delaminations are produced radial cracks are seen where the sharp edges of the Berkovich tip made contact. With the conical tip, a one dimensional analysis of the circular blister can be used as it is assumed that the load distributed by the indenter tip will be equal all around the blister. With the Berkovich tip, this assumption may no longer be true and a different approach needs to be taken in calculating the strain energy release rate.

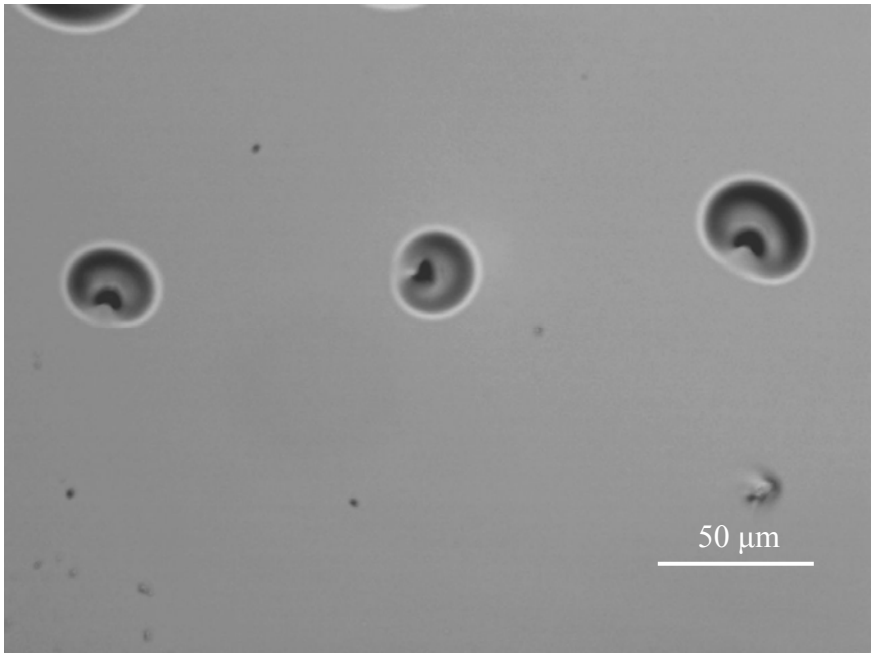

Figure 32. Asymmetrical delamination blisters made with Berkovich tip.

3.4 Double indent test

The superlayer indentation test was slightly modified to introduce water at the film/substrate interface to be able to quantify film adhesion in a wet environment. An initial indent was made to a depth equal to the thickness of both the superlayer and the film of interest. De-ionized water was then placed in the area where the initial indent was made using a volumetric pipette. A second indent was made in the same spot as the first one, but to a larger load, thereby supplying additional energy to drive film delamination. The same approach was taken in the single indent tests, for determining the blister radius and the plastic indentation depth in the double indent test.

A double indent was first performed on the 67 nm thick copper film in the dry environment and compared to a single indent at the same maximum load in a dry environment to see what effect was caused by double indent process on adhesion

measurements. It can be seen in Figure 33 that the loading and unloading curves for both the single indent and double indent made to the same maximum load in a dry environment do not match up, since the the Hysitron Triboindenter® does not record changes in load and displacement until initial contact is made. The 300 nm shift to the right for the double indent was applied after the indentation process. The shift amount was taken as the final depth of the initial indent.

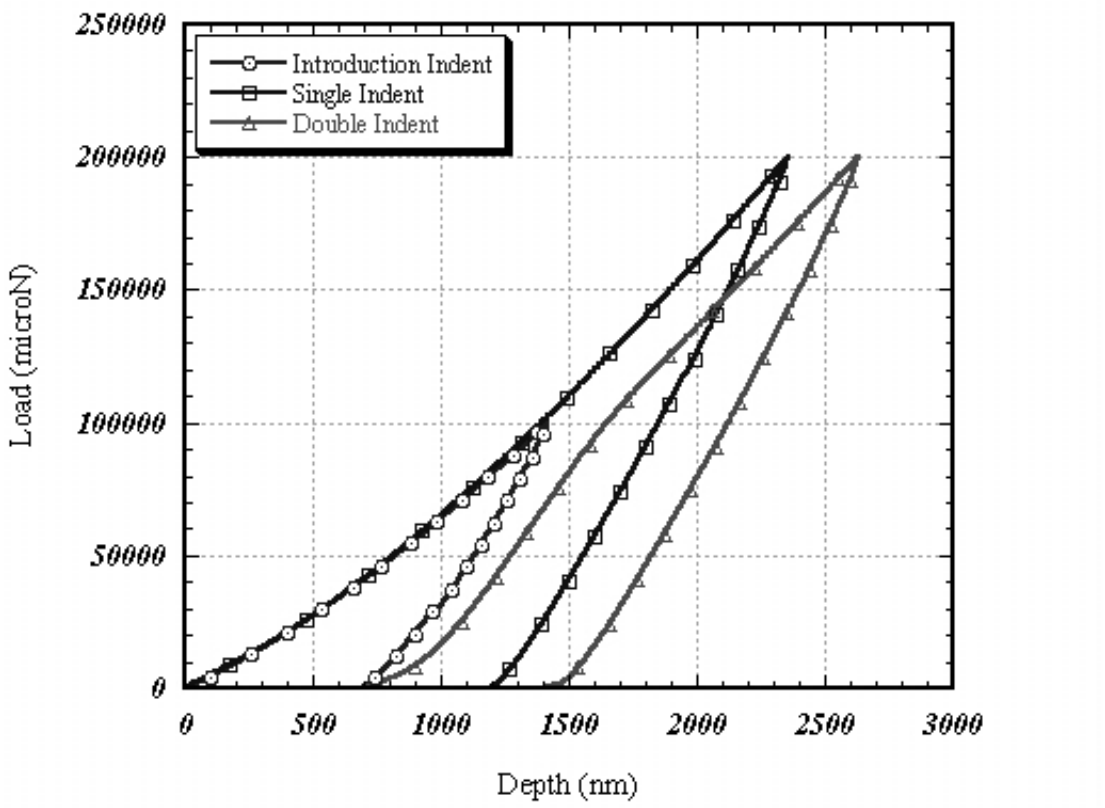

Figure 33. Double indent versus single indent in dry environment.

Not only is it apparent that the double indent procedure went deeper than the single indent, but the final delamination blister radius for the double indent was 2.5 μm larger than the single indent to the same maximum load. Both delamination blister radius and plastic indentation depth are used in calculating the strain energy release rate. When the strain energy release rate was calculated for the double indent in the dry environment,

it was found to be the same as single indents with the same x/a ratios (Table 3). These findings prove that the double indent procedure has no effect on changing the outcomes for measuring film adhesion.

The strain energy release rate measurements in Table 3 provide sufficient evidence that the double indent procedure has little or no effect on the film adhesion measurements. The variation shown for the double indent procedure falls within the variance observed for taking measurements with a single indent.

Table 3. Double and single indent adhesion results in dry environment.

Indent Procedure	Maximum Load (mN)	x/a	G (J/m^2)
Double Indent (Dry)	200	7 - 8	7.8 ± 0.3
Single Indent (Dry)	225 - 250	7 - 8	8.1 ± 0.5

3.5 Adhesion measurements in a wet environment

Since the double indent procedure produced no discrepancies in measuring film adhesion in the dry environment, the effects of water on film adhesion were clearly evidenced. Measuring copper film adhesion in the wet environment was successful from the first conducted test, as larger delamination blister radii were immediately noticed with the introduction of water. In regard to the DLC film there was an apparent effect of water on film adhesion. Unfortunately the delamination blister shape was not circular, as the initial tests on the DLC film produced telephone cord delaminations immediately upon the introduction of water (Figure 34).

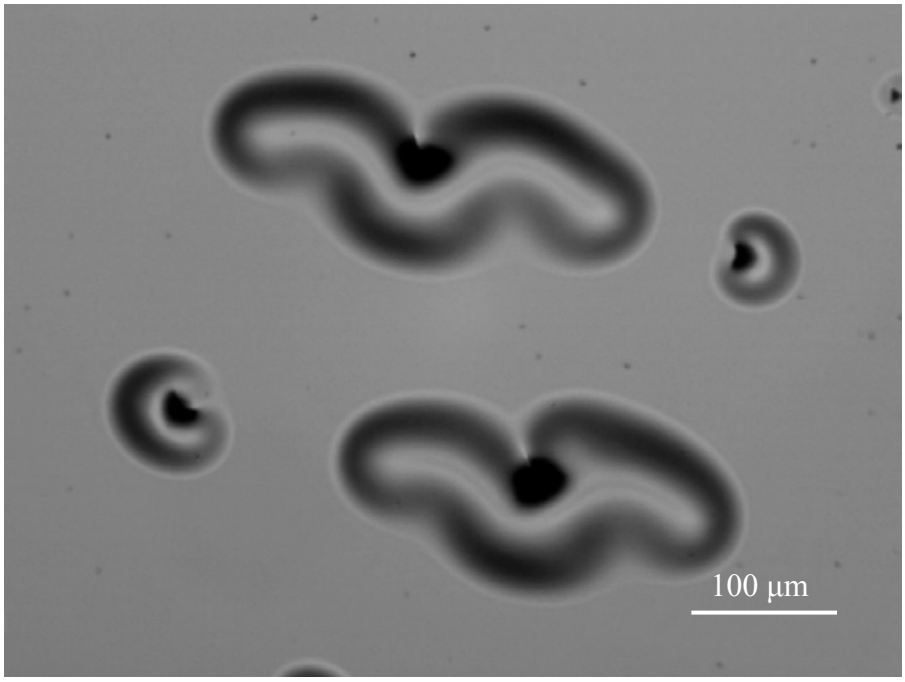

Figure 34. Telephone cord delamination induced in DCL film by water and indentation.

Telephone cord delamination blisters (Figure 35) have been observed when the compressive residual stress of the film was at least a factor of 8 greater than the critical buckling stress of the film [1, 38, 50, 51]. As soon as the water was removed from the DLC film the telephone cord delaminations would stop propagating. Even though circular blisters were not initially present to calculate the adhesion of the DLC films in a wet environment, there was an apparent effect of water reducing the adhesion of the DLC films.

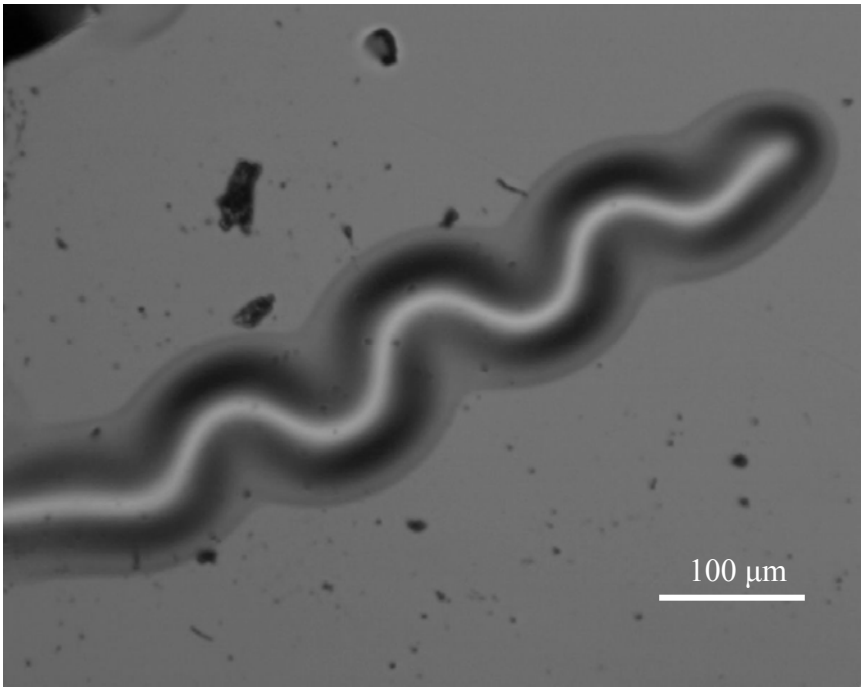

Figure 35. Telephone cord delamination.

For the copper thin films, much larger radii measurements were taken in the wet environment compared to indents of the same maximum load in the dry environment (Figure 36). In Figure 36 150 mN indents were performed on the 67 nm thick copper film in dry and wet environments. The difference in blister diameters is obvious and radial cracks can be seen on the right blister. Telephone cord delaminations were never seen with the copper films, unlike with the DCL films, therefore blister radius and plastic indentation depth were immediately taken to calculate film adhesion.

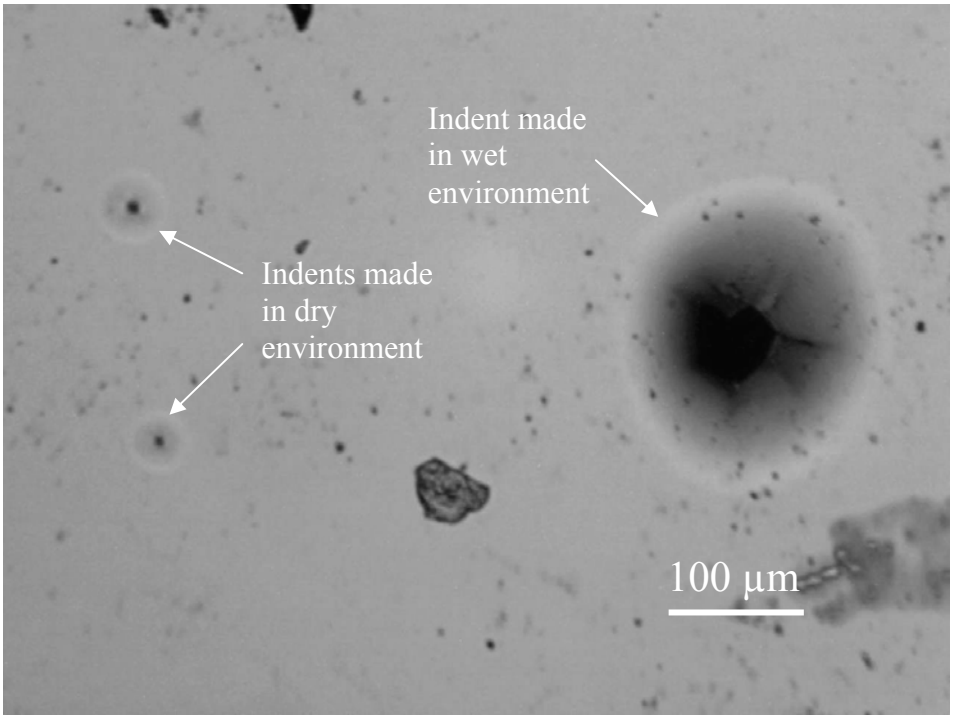

Figure 36. Indents in the 67nm thick copper film in dry and wet environments.

For the DLC film in the dry environment the range of the maximum loads was from 200 to 400 mN. When the double indent procedure was first attempted in the wet environment the introductory indent was made to a maximum load of 200 mN and the second indent was made to a maximum load of 250 mN. After the introductory indent was dropped down to a maximum load of 150 mN and the second indent was changed to a maximum load of 200 mN, telephone cord delaminations no longer appeared. If the introductory and second indent loads were dropped any lower there were no observed changes in size of the delamination blisters. No changes were observed because water was not able to reach the interface, as the indentation depth was too shallow and the film stack was not penetrated (Figure 37). The load range was more restricted during the

double indent test for the DLC film than the copper films due to the telephone cord delaminations appearing upon the introduction of water.

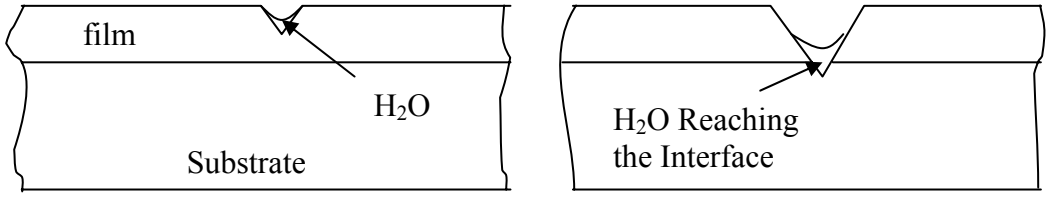

Figure 37. Schematic of necessary penetration depth for water to induce delamination.

Symmetric blister shapes that were seen for the 67 nm thick copper film, were not seen for the 97 nm thick copper film and the DLC film. Lower film adhesion, residual to buckling stress ratio (σ_r/σ_B) and biaxial stress conditions are thought to be the contributors to the asymmetrical blister shapes. For elliptical shaped blister in the wet environment, the radii were recorded in both the major and minor radial directions, then averaged to calculate adhesion (Figure 38).

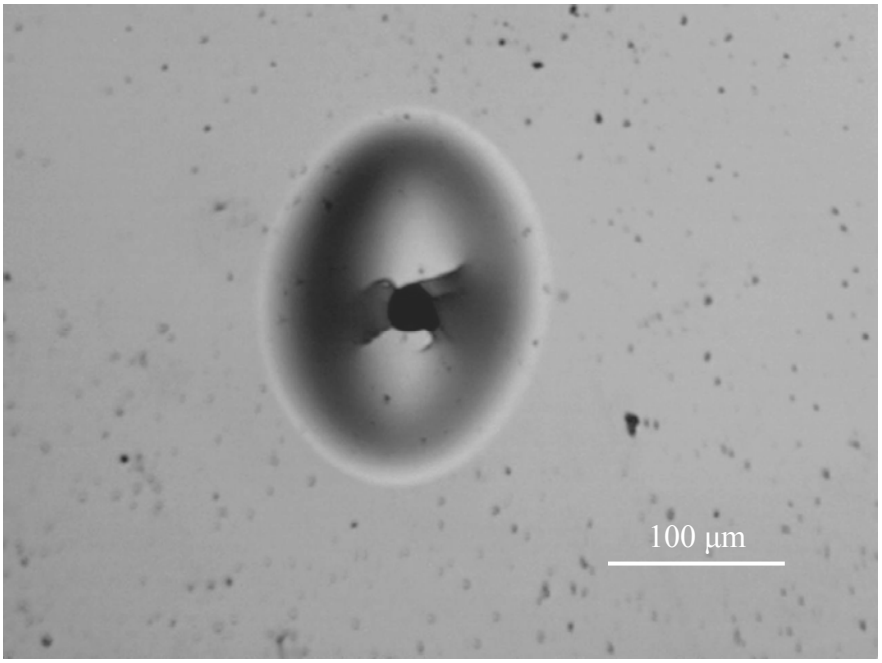

Figure 38. Asymmetrical blister shape of the 97 nm thick copper film.

Adhesion measurements in the wet environment for both samples of copper showed a reduction in adhesion by a factor of 10 to 20 compared to those performed in the dry environment. For the 67 nm thick copper sample the average adhesion in a wet environment was 0.15 J/m^2, and for the 97 nm thick sample the average adhesion value in a wet environment was 0.10 J/m^2. For both copper samples, the blister diameter for a 150 mN indent in the dry environment was approximately 20 μm and increased up to 150 μm when the double indent was made in the wet environment. The DLC film adhesion dropped by a factor of 50 to 60 in the wet environment and was measured to be 0.015 J/m^2. Table 4 compares film adhesion and blister sizes for the same maximum loads in dry and wet environments.

Table 4. Adhesion of thin films in wet environment.

Sample	Blister Diameter (μm)	G (J/m^2)
Cu 67 nm (Dry)	20 ± 5.0	2.74 ± 0.86
Cu 67 nm (Wet)	150 ± 15	0.15 ± 0.05
Cu 97 nm (Dry)	20 ± 5.0	1.98 ± 0.82
Cu 97 nm (Wet)	150 ± 20	0.10 ± 0.01
DLC (Dry)	15 ± 5.0	2.09 ± 0.31
DLC (Wet)	100 ± 20	0.035 ± 0.015

Figure 39 shows a load-displacement curve for a double indent made in the wet environment for the 97 nm thick copper film. An introductory indent made to a maximum load of a 100 mN and a second indent to a load of 150 mN, compared to a single indent made in a dry environment to a maximum load of 150 mN.

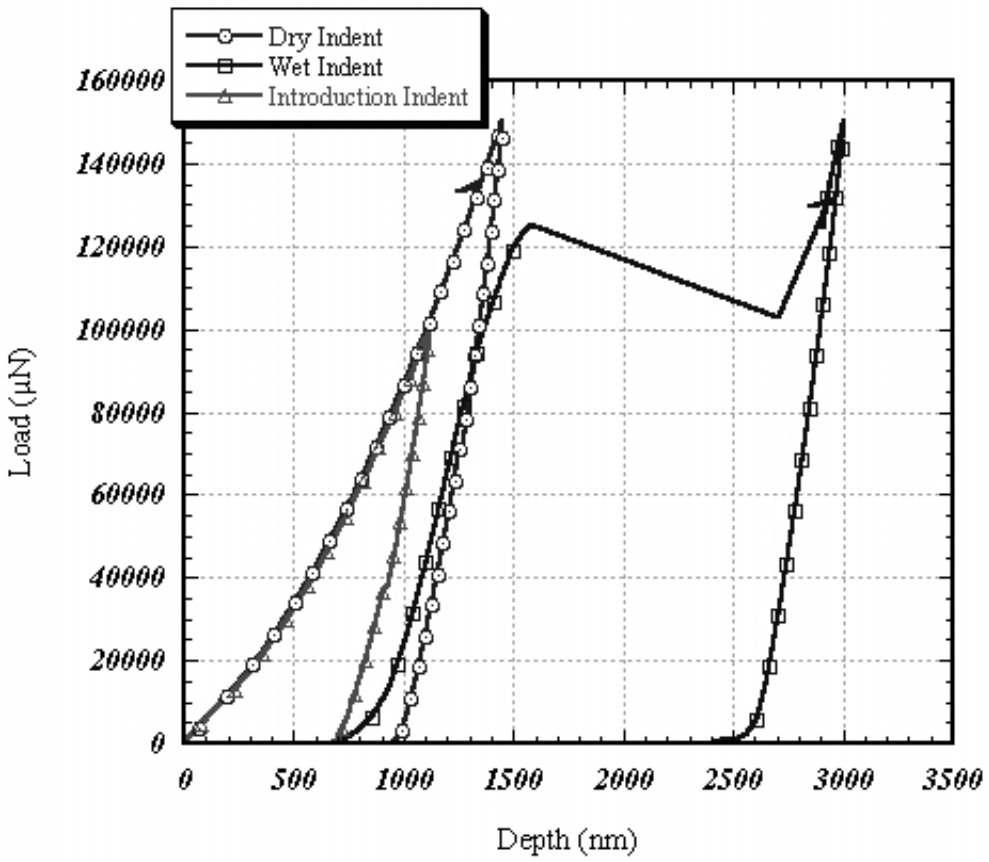

Figure 39. Double indent in wet environment.

3.6 Substrate fracture and film buckling

Not only did blister radius and indent depth drastically change with the presence of water, but the load excursions dropped dramatically. In the dry environment, load excursions were observed at approximately 275 mN. However, in the wet environment load excursion happened at approximately 125 mN (Figure 40). The loads at which these excursions happened, were always the same.

Every time these load excursions have been observed, extensive cracking of the buckled film and the substrate was observed. The radial cracks in the buckled thin film start at the indent in the center of the delamination blister and move outward. Fractures in the substrate were always observed at 90º angle from each other (Figure 41).

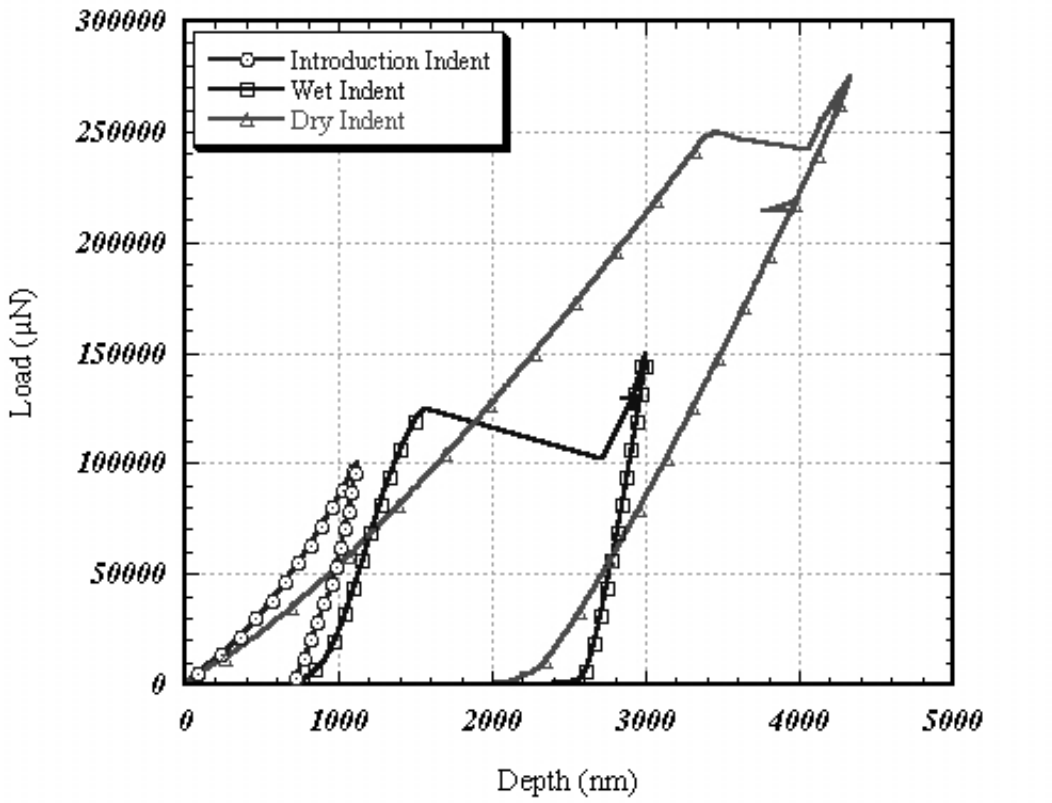

Figure 40. Load excursions in wet and dry environments.

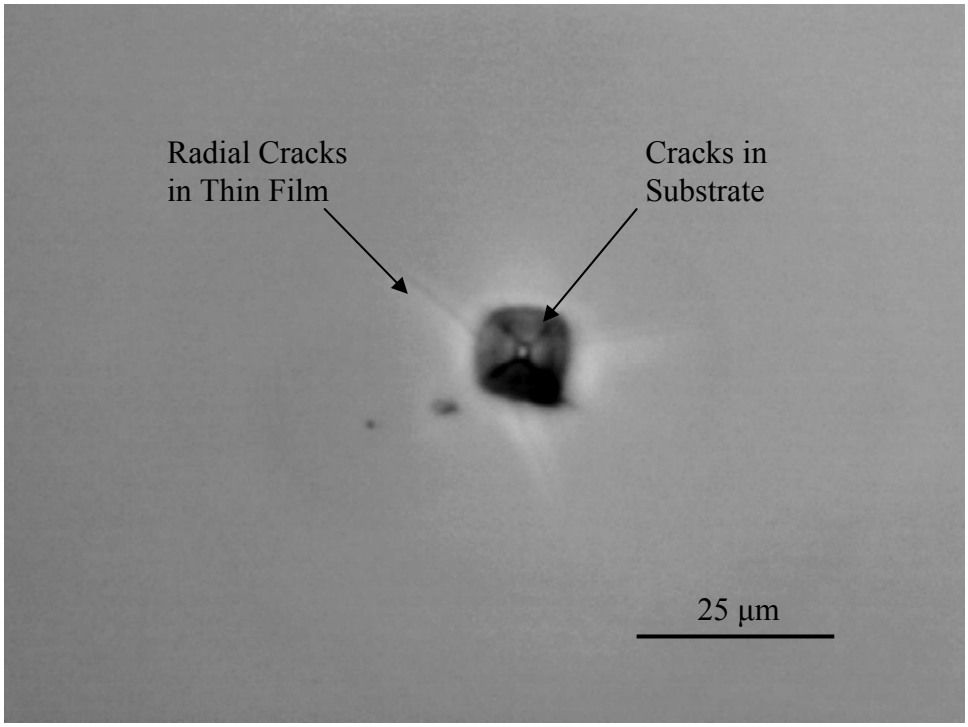

Figure 41. Substrate and film fracture patterns.

3.7 Reduction in adhesion

It is apparent that with the introduction of water, film adhesion drops and crack propagation rates increase. Until now, only changes in crack propagation rates as the result of an introduction of moisture has been quantified [17, 20, 21]. With such high values of compressive residual stress present in the copper and DLC films, only a small reduction in interfacial toughness is required to drive debonding of the film from the substrate. For the DLC films an introduction of water at the crack tip was enough to drive interfacial cracking further, but for the copper films an additional driving force was needed to propagate interfacial cracking. This could indicate that there is greater residual stress in the tungsten superlayer of the DLC film.

For the copper samples, oxidation may be taking place with the introduction of water at the film/substrate interface, unlike for the DLC film. No evidence has been found that DLC films will chemically react with water. Moisture effects in DLC films have only been reported to increase their frictional properties. A pull off test was conducted to measure the effects of water on DLC film adhesion, but no change was reported [52]. This test may be faulty, however, as no evidence was shown that water was present at the film/substrate interface. Water may be lowering the surface energies at the interface, which may be enough in combination with capillary pressure and high residual stresses to drive interfacial debonding of DLC films.

It is thought that copper films may have similar chemical reactions with water as bulk glasses and Ta/SiO_2 interfaces [17, 53]. For bulk glasses, the chemical reaction at the crack tip is due to water molecules absorption by the strained Si-O bonds [21]:

$$H_2O + Si\text{-}O \rightarrow 2SiOH \qquad (42).$$

Upon debonding at the Ta/SiO_2 interface, Ta is expected to be oxidized following the reaction [53]:

$$2Ta + 5\ H_2O \rightarrow Ta_2O_5 + 10H^+ \quad (43).$$

Copper oxidation was seen at elevated temperatures as a result of chemical-mechanical polishing (CMP) [54-56]. At ambient conditions, it is still thermodynamically favorable for a thin layer of oxide to form on the surface. Two possible copper oxides that may form are cuprous and cupric oxides:

$$Cu + O_2 \rightarrow Cu_2O$$

$$2Cu + O_2 \rightarrow CuO \quad (44).$$

Cu_2O is more likely to form at low temperature, but small amounts of CuO could also form. It has been shown that copper oxide lowers thin film adhesion [56, 57]. Copper oxide is approximately twice as hard as pure copper, so reduction in adhesion is expected.

Copper oxide at the interface may restrict the amount of plasticity around the crack tip. If that is the case, less energy would be dissipated by plastic deformation and more energy would be used in creating two new surfaces. Usually, the thicker the metal film, the more plastic deformation can take place, which will lead to higher adhesion values [46, 47, 53, 58].

Proof that copper oxidation can occur at the film/substrate interface was discovered when trying to solve copper diffusion problems [54]. A particular concern with copper technology is that copper may interact with interlayer dielectric material to degrade the interface and lead to a loss of adhesion. Copper transport into the dielectric material may also cause line-to-line leakage or electrical short circuits [59]. It has been

concluded that copper by itself will only diffuse into dielectric layers at elevated temperatures and/or with an applied voltage. Tests showed that high concentrations of O_2 or water present at the SiO_2 surface form a thin layer of copper oxide, which acts as a source of copper ions. These copper ions have been seen to then transport through the SiO_2 at low temperatures and electric fields less than 1.0 MV/cm [54]. The transport of copper ions is a verification that a thin layer of copper oxide is formed in the presence of O_2 or water.

In conclusion, results have shown that water significantly reduces film adhesion. The primary reason for a reduction in film adhesion is thought to be due to a lowering of surface energy at the crack tip. Lower film adhesion may also be affected by surface oxidation and contaminants in the water. Oxidation of the copper film was supported by past findings for a Ta/SiO_2 interface [53]. Additional studies will be taken to further explain possible crack tip reactions for the DLC film. The telephone cord delaminations as a result of water introduction to the DLC film will be discussed next.

CHAPTER 4

FLUID TRANSPORT THROUGH DELAMINATIONS

4.1 Telephone cord delamination propagation

When the amount of stored elastic energy in a thin film due to the residual stress exceeds the interfacial toughness, fracture normally occurs. For the DLC film, equi-biaxial film stress may be partially relieved by either straight-sided blisters or telephone cord propagation. For the 5 nm thick DLC film used in the indentation tests, telephone cord delaminations were observed and straight-sided blisters were seen in a second sample provided by Seagate that had a 20 nm thick DLC film. However, there were no straight-sided or telephone cord delaminations noticed on the copper samples. Telephone cord blisters occur by "secondary" blister buckling perpendicular to its propagation direction, which results in the sinusoidal fracture patterns. If the compressive residual stress is at least 4 times the buckling stress, telephone cord morphology is commonly observed [1, 29, 38, 50, 51, 60]. Recent studies have been conducted to predict buckling patterns [29, 60]. This was accomplished by creating an experimental setup where factors such as film stress, thickness and interfacial adhesion were controlled.

Moon and colleagues have been able to control the buckling parameters by using lithographic techniques to create areas of low adhesion on substrates [29]. On a macroscopic level buckling patterns were controlled by gluing a polycarbonate strip to a

PVC block and applying forces in two directions using screws (perpendicular and parallel to the strip) [60]. For both methods a residual to buckling stress ratio of $\sigma_r/\sigma_B = 5$ produced straight-sided or Euler blisters, $\sigma_r/\sigma_B = 6.5$ predicts bumps or varicose blisters and for $\sigma_r/\sigma_B = 7.5$ telephone cord blisters would appear (Figure 42). For the experiment, where the biaxial stress could be controlled, various buckling patterns appear when the stresses perpendicular and parallel to the film strip were not equal.

When the stress perpendicular to the film strip (transverse) was much larger than the stress parallel to the film strip (lateral), the straight-sided blister would always appear. If the lateral stress was much larger than the transverse stress, bumps or varicose blisters would form. For combinations in between, where stresses were not equi-biaxial, a combination of a telephone cord and varicose blister would form [60].

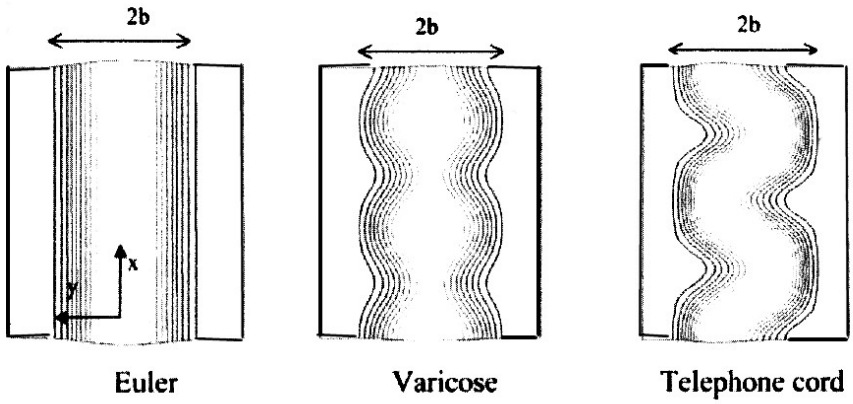

Figure 42. Buckling patterns in compressed films [60].

If the profile of a straight-sided blister is taken, the derivations made by Hutchinson and Suo for a one-dimensional blister can be used to calculate thin film residual stress, buckling stress and strain energy release rate (Figure 43) [13].

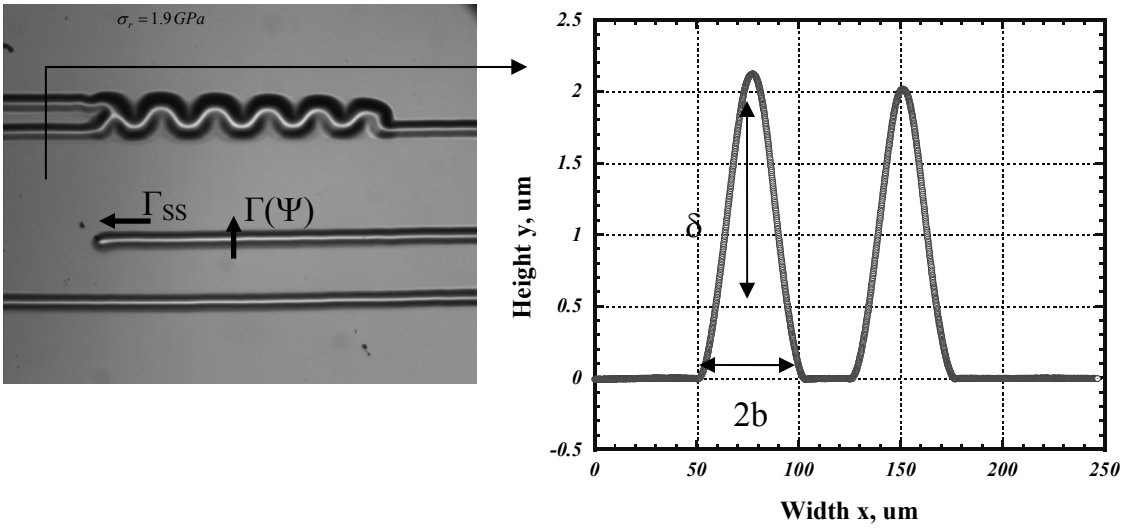

Figure 43. Blister height profile.

Recalling equations that were presented in Chapter 2 and using the blister height profile in Figure 43, the critical buckling stress in the 20 nm thick DLC film with W superlayer was calculated to be 365 MPa (Equation 29). Knowing the film thickness, the straight-sided blister height and using the critical buckling stress, the residual stress of the film was calculated to be 1.9 GPa (Equation 30). The calculated value of residual stress of 1.9 GPa confirms the measured value for residual stress using the wafer curvature technique. Calculating the σ_r/σ_B ratio for the 20 nm thick DLC film to be 5.4, agrees with the Moon and Audoly findings for predicting straight-sided buckling patterns in compressed films [29, 60].

With the found residual and critical buckling stresses, the strain energy release rate in the buckling direction was calculated to be 4.66 J/m^2. This value is in agreement with the indentation result of 5.5 ± 0.2 J/m^2 for the 20 nm thick DLC film.

For straight-sided blisters the strain energy release rate can also be found in the direction of crack propagation [13]:

$$\Gamma_{ss} = \frac{(1-\nu^2)h\sigma_r^2}{2E}\left(1-\frac{\sigma_B}{\sigma_r}\right)^2 \qquad (45),$$

The strain energy release rate in the direction of blister propagation in the 20 nm thick DLC film was calculated to be 2.45 J/m^2.

Normally these straight-sided or telephone cord blisters "run out of steam" and stop once the interfacial toughness exceeds the strain energy release rate. It is possible to make blisters propagate further by either applying mechanical energy to the system, or by introducing liquids at the crack tip, thus reducing the film interfacial toughness.

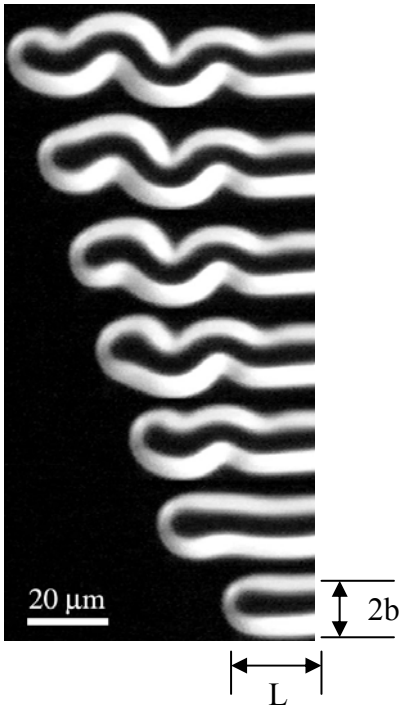

Figure 44. Transition from straight-sided blister to sinusoidal shape.

Straight-sided blisters will precede the sinusoidal pattern until a critical length is reached. For films with $\sigma_r/\sigma_B =$ 6.5 Moon has recorded the onset of a sinusoidal pattern to start appearing when the ratio of blister length to width (L/2b) equals 0.96 [29].

The transition from a straight-sided delamination to a telephone cord delamination is shown inFigure 44. Here sinusoidal transition is observed with a L/2b ratio of approximately 1.67 [38].

It has been shown that telephone cord delaminations can be forced to propagate by applying mechanical forces [38]. Similar blister propagation has been observed with the introduction of water. To induce telephone cord propagation by the introduction of water, the samples were first mounted to a stage of an optical microscope by a small amount of adhesive. Since the samples were scribed from a 4-inch wafer, small blisters were randomly present at the edges of the samples. After an edge of the sample was located with blisters present, water was placed on the stage in contact with the edge of the sample. Delamination of DLC films was immediately seen when the water came into contact with the edge of the sample. In Figure 45, propagation is seen for the blister coming from the top, where distilled water was introduced. Growth was not noticed in the bottom blister where no fluid was present. Propagation of the telephone cord delaminations continued until the water was taken away from the sample, or the blister reached the film edge on the opposite side of the sample.

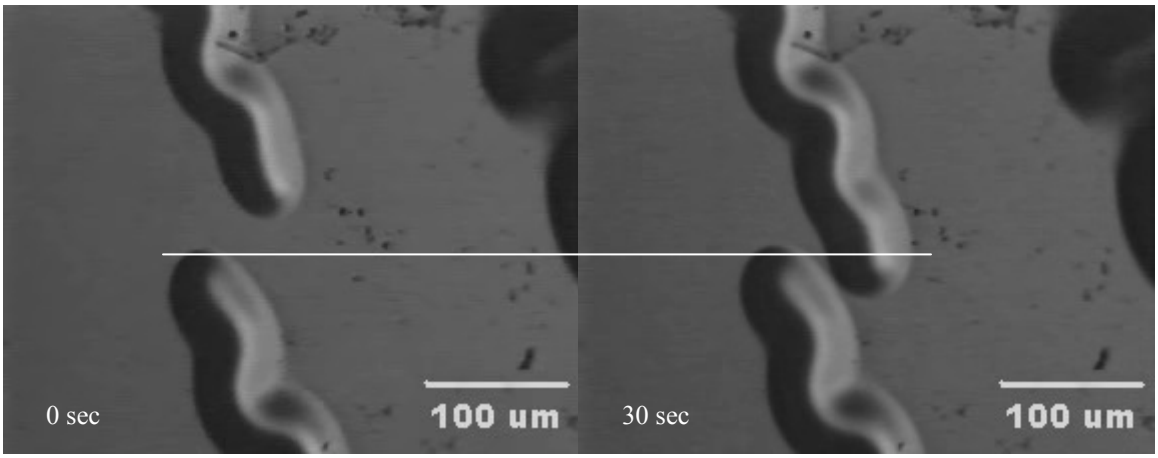

Figure 45. Telephone cord propagation induced by water introduction.

In Figure 46 water exiting the delamination is observed, which proves that water is present at the crack tip and is contributing to the telephone cord blister propagation. Comparing the two images, water is seen flowing from the opening in the delamination and is moving some of the small loose fragments of the thin film. The delamination size has also increased. In this experiment distilled water was introduced on the right side of the sample and forced a telephone cord delamination until it had reached the film edge on the left side of the sample.

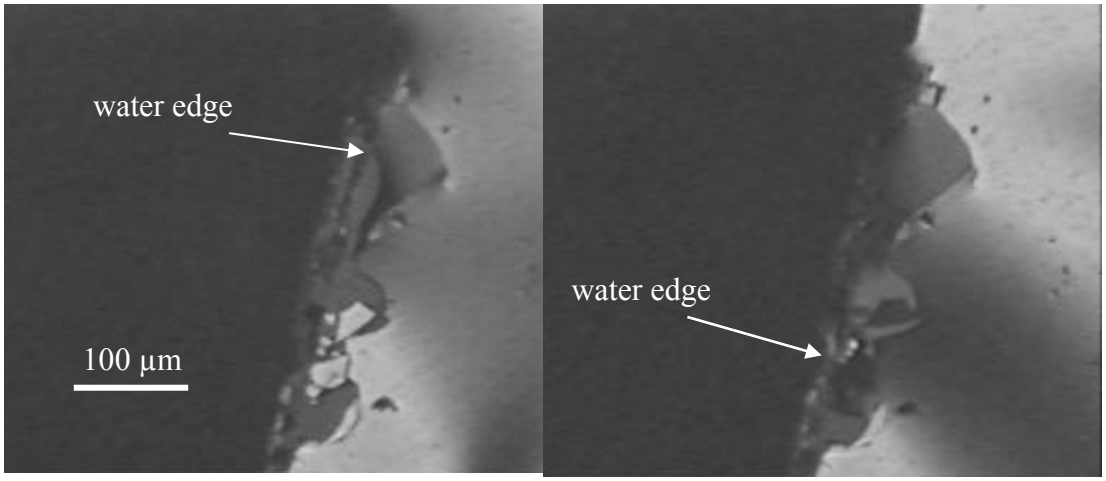

Figure 46. Water exiting a telephone cord delamination.

In addition to distilled water, tap water, alcohol and various oils were tried, and corresponding propagation rates are listed in Table 5. Propagation rates were measured to be the same for distilled and tap water (pH = 7). Water temperature effects were also tested in the range of 22°C to 72°C. However, very little difference in propagation rates was noticed in this temperature range. Results for the water temperature effects on the DLC film showed propagation rates decreasing with an increase in temperature. These results contradict findings of Lane and Dauskardt for TaN/SiO_2 films where propagation rates were observed to increase with an increase in temperature [53]. Their findings

would indicate a temperature-dependent chemical reaction was taking place at the crack tip for the TaN/SiO_2 interface, but amorphous carbon films are chemically inert [43, 44].

The same localized effects on adhesion due to variations in residual stress seen during indentation tests, were also observed during crack propagation rate measurements. Propagation rates for the 5 nm thick DLC sample would change with each new scribed piece. For testing the effects of temperature and different liquids, a sample with many edge blisters was chosen. This was done so that numerous tests could be performed on the same sample piece. The average size for the scribed sample was approximately 1 x 1 cm^2.

Table 5. Propagation rates of various fluids in DLC sample.

Fluid Type	Propagation Rates (μm/sec)	Re
Isopropyl Alcohol	0	-
Oil	0.083	1.3×10^{-8}
Distilled Water	3-5	2.5×10^{-4}
22°C Tap Water	3-5	2.5×10^{-4}
72°C Tap Water	2.5	1.2×10^{-4}

Figure 47 shows the propagation of a telephone cord delamination where water was introduced on the left side. Frequently, many telephone cord blisters would form in close proximity to each other with a spacing of 1-2 microns. Merging of telephone cord delaminations was only noticed when delaminations were propagating from opposite directions (Figure 45).

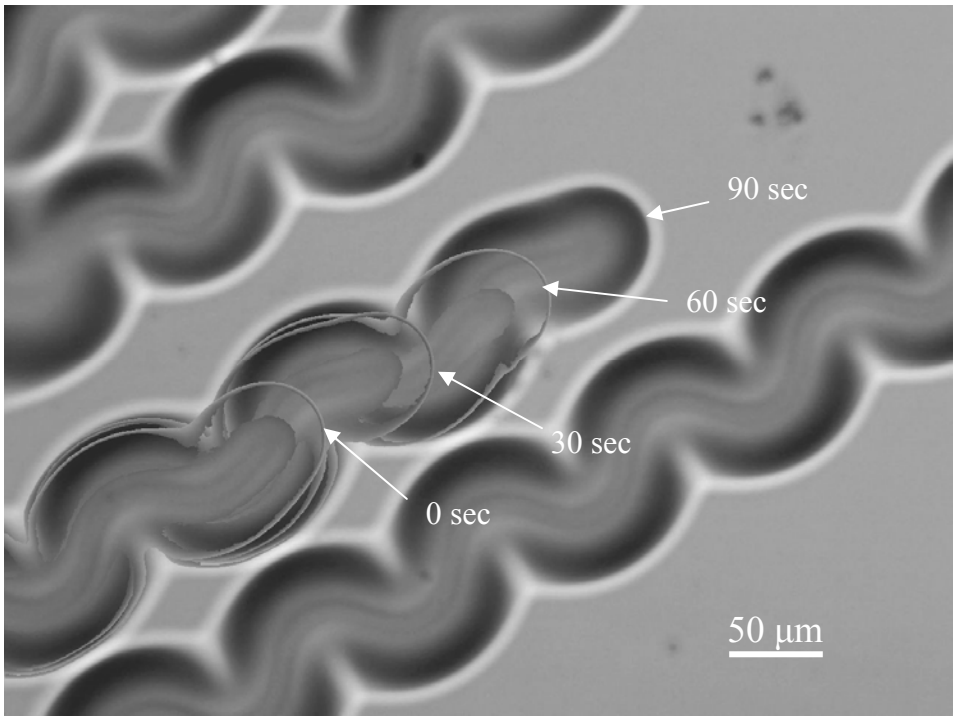

Figure 47. Telephone cord propagation.

4.2 Microfluidic application of telephone cord delamination blisters

Microfluidics as a field has been growing with the new advances in nanotechnology [61]. In fact, this field has been estimated to grow at a near exponential rate in the decades to come. This relatively new technology has been considered for many different possible applications in the biomedical field, including drug delivery. For example, pharmacological agents could be successfully delivered directly to the wound sites [62]. This potential technology relies on the ability to transfer fluids through microchannels. Channels with at least one dimension less than 1 mm, are usually considered in microfluidics. As a result of microchannels small dimensions, the Reynolds number is often much less than 1. The Reynolds number is defined as:

$$\mathrm{Re} = \frac{VL}{v} \qquad (46),$$

where V is the flow velocity, L is the channel width and v is the kinematic fluid viscosity. For the maximum propagation rates seen with water, and using the blister profile in Figure 43, the Reynolds number in the telephone cord delamination is calculated to be 2.5 x 10^{-4}. With such a low Reynolds number, flow is completely laminar and no turbulence occurs. Microchannels are commonly etched in silicon by means of standard methods of lithography, but because of the multiple steps involved, the whole process is cumbersome, expensive, and labor intensive [63]. Delamination blister on the other hand, have been created easily and act as microchannels for fluid transport.

Figure 46 shows that a fluid can not only spur delamination propagation, but will also exit the delamination if the blister opens up. If the direction of the blisters growth could be controlled, telephone cord delaminations could be used as microfluidic channels. Substrate patterning to control thin film adhesion has been accomplished [29], and may find uses in microfluidic devices if combined with the fluid transport described here. One disadvantage of using the telephone cord delaminations as a fluid transport mechanism, would be its one-time use.

If telephone cord delaminations were to be used as open channels, fluid flow pressure would have to be kept low. Some microdevices produce enough pressure to cause total failure of the film. Telephone cord delaminations have shown some stability though, as in Figure 48 they are being manipulated with a tungsten microprobe. If the flow pressure could be controlled, micropumps could be used to force fluid through the open delamination channels.

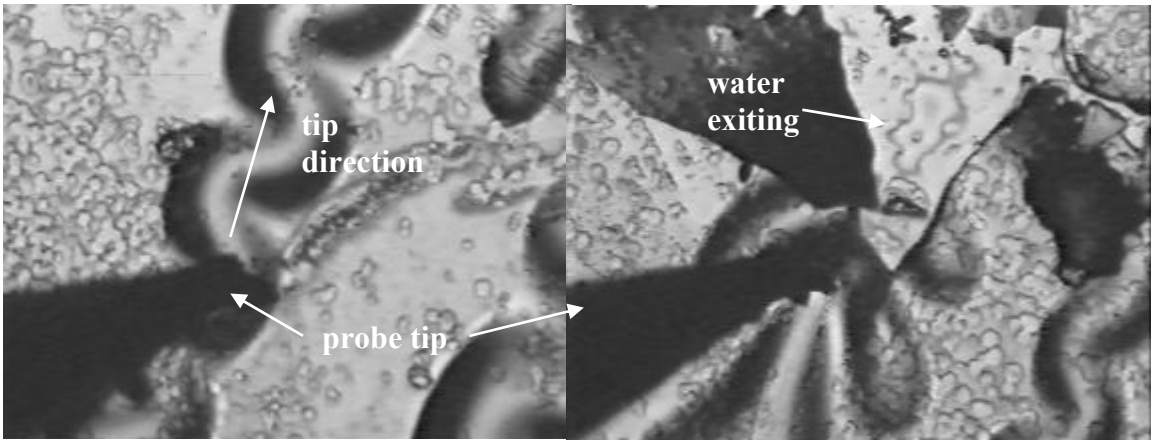

Figure 48. Microprobe manipulation of telephone cord delamination.

In order to manipulate telephone cord delaminations, a microprobe was set up on an adjustable rigid stand, adjacent to an optical microscope. The microprobe stage had the ability to be moved in the X, Y and Z directions (Figure 49). In Figure 48 the microprobe was first used to tear a small hole in the thin film so that the substrate was exposed. Water was then introduced to the edge of the sample to propagate telephone cord delaminations in the direction of the thin film tear. A small amount of water could be seen exiting the delamination when it reached the tear. By pushing the delamination with the microprobe towards the tear, water could be forced out of the delamination, and appeared on the substrate. By reversing the direction of the microprobe motion, fluid flow was reversed and water was forced back out of the original delamination.

When the applied forces of the microprobe were kept low enough, delamination blisters remained intact. If micropumps were attached to the delamination channels, fluid could be successfully pushed through without creating further interfacial cracks.

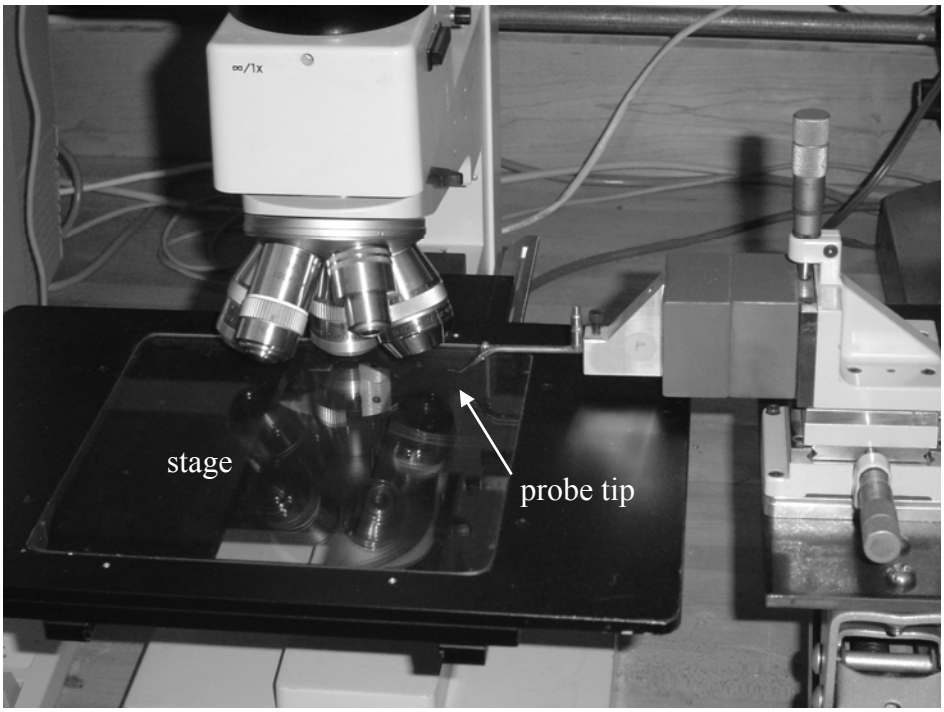

Figure 49. Microprobe setup.

4.3 Fluid flow in microchannels

It is predicted that there is a small pocket of air trapped at the crack tip when a fluid is introduced to a crack. [17]. The pocket of air present at the crack tip will produce a three phase interaction similar to Figure 50.

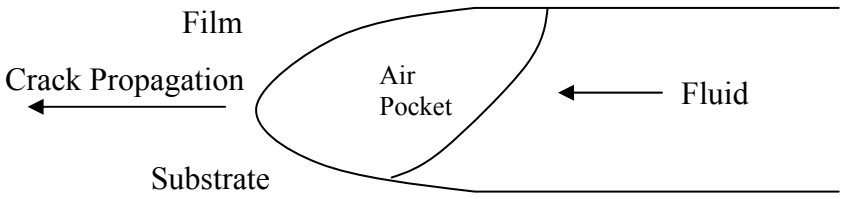

Figure 50. Fluid flow in delamination channel.

For contact angles less than 90º, the fluid wets, meaning it is more attracted to the solid surface and not to itself or the air. If this condition exists, the solid surface is said to

be hydrophilic and it will produce a capillary force in the delamination channel. The capillary force on the fluid in a microchannel, due to the air/liquid/solid interface interactions, can be calculated using the following equation:

$$F = 2\pi \cdot r\sigma \cos(\theta) \quad (47),$$

where r is the channel radius, σ is the interfacial tension between air and liquid, and θ is the contact angle defined earlier. For fluid flow in microchannels this effect is represented as an equivalent pressure, or capillary pressure:

$$\text{for circular tubes: } P = \frac{2\sigma \cos\theta}{r} \quad (48),$$

$$\text{for rectangular tubes: } P = \sigma \cos\theta\left(\frac{1}{h} + \frac{1}{w}\right) \quad (49),$$

where h and w are the depth and width of the microchannel, respectively. These equations demonstrate that for larger contact angles there is a decrease in force or pressure and therefore a decrease in flow rate. This can explain why water worked so well for flowing through the telephone cord delaminations, but the various types of oils did not. Water has a smaller contact angle θ than oil does. Water was able to easily flow in the channels, while oil did not flow without external assistance. Just by applying a mechanical pump to drive fluid flow in microchannels may not be enough, since pumps will not change the capillary forces. Non-mechanical pumps work very well by adding an electrical potential, or a temperature difference that will help fluid flow by creating a change in the contact angle [64, 65]. Since fluid flow is dominated by the nature of the channel surface, different materials could also be used to control the fluid flow. It has been shown that silver on channel surfaces will increase the contact angle of water by 20°

and by 27° for methanol, stopping capillary or external pressure-driven fluid flow in typical microchannels [66].

CHAPTER 5

SUMMARY AND FUTURE WORK

5.1 Summary

The effects of water on thin film adhesion and telephone cord delamination propagation rates have been studied. Film adhesion in a wet environment was quantitatively measured for copper and amorphous carbon films. Copper films have shown a drop in adhesion by a factor of 10 to 20, and the DLC film adhesion was reduced by a factor of 50 to 60. A reduction in adhesion is primarily thought to be due to lowering the surface energy at the crack tip. Lower film adhesion can also be affected by surface oxidation and contaminants in the water. Future studies should be conducted on various types of films to further explain the interaction of water at the film interface. Additional experiments will provide a better understanding of environmental effects in thin films.

5.2 Various environmental effects

The effect of moisture on film adhesion and delamination was the primary goal of this thesis. Temperature effects on the delamination propagation rate were also considered for a relatively small temperature range, which should be expanded. Delamination propagation rates of the DLC film slowed down when water temperature was increased from 22 ºC to 72 ºC. Slower propagation rates would indicate higher film

adhesion which agrees with past studies of metal and polymer films [39, 67]. Previous tests on copper films have shown an increase in adhesion with temperature increasing from 23ºC to 130 ºC. The adhesion of ethylene-styrene copolymers to polyethylene has also increased with increasing temperature, but only in a small temperature range. The reason for an increase in adhesion is thought to be due to lowering of the yield strength of the film, therefore increasing the amount of plastic deformation at the crack tip.

With the growing use of copper in microelectronics, copper films must be able to withstand the various fabrication and cleaning processes involved in microelectronics manufacturing. Future experiments will be formulated to observe the effects of varying pH levels on copper film adhesion.

5.3 Radial cracking

Radial cracking was observed at larger indentation loads during the superlayer indentation test. Film cracking may lead to problems in calculating the strain energy release rates, as the current analysis does not account for film and substrate cracking. One possible way to introduce radial cracks is to modify the buckling solution to account for a pie slice geometry instead of a full circular plate. Future modeling on a macroscopic level as well as finite element analysis of a delamination blister may lead to a relation in the load excursions seen in the load-displacement curves to film and substrate fracture.

5.4 Biaxial film stress

For a one-dimensional or straight wall buckle, it is assumed that the equi-biaxial film stress is present when solving for the strain energy release rate. After indents were

made in a wet environment for the 97 nm thick copper film and the 5 nm thick DLC film, asymmetrical blister shapes were observed. These findings may indicate that equi-biaxial stress is not present. To confirm this, a second indent will be performed where the sample would be rotated 90º relative to the first indent. If the blister shape of the second indent is still elliptical with the major radius of the ellipse in the same direction as the first blister the residual film stress would not be equal to the stress in both principal directions. Radii measurements will be taken to find out what the stress relation is in the x/y-axis directions and confirmed with X-ray diffraction.

5.6 Microfluidic applications

After observing the potential for fluid transport in delamination channels, the usefulness of delamination channels in microfluidic devices will be tested. The main issues to consider are the control and stability of the delaminations for fluid transport. Delamination size and direction have been successfully controlled by lithographic techniques [29]. To control fluid flow the possibility of different types of micropumps and integration of delamination channels into MEMS devices will be examined.

There are two choices of pumps to pick from, mechanical pumps and non-mechanical pumps. Mechanical pumps can be broken up into two categories based on the manner in which energy is supplied to them: displacement pumps and dynamic pumps. In displacement pumps energy is periodically added by the application of force to one or more moveable boundaries, resulting in pressure increase. In dynamic pumps the energy is continuously added to increase fluid velocities within the machine. Disadvantages of the mechanical pumps are the complexity involved with the manufacturing of the pump and the relatively large size and high flow rates. Mechanical

pumps may not work with the delamination channels unless increased delamination stability is achieved.

Non-mechanical pumps have their advantages in their use at the microscale and their ability to change the capillary force of a fluid. They add momentum to the fluid by converting another non-mechanical energy form into kinetic energy. Some common types of non-mechanical pumps include electrical pumps, surface tension driven pumps, chemical pumps and magnetic pumps. Telephone cord delaminations themselves are surface tension driven pumps.

5.7 Crack propagation rates

Many of the current publications that review the effects of moisture on thin films are using the four-point bend test. The four-point bend test has a major advantage in the fact that the applied strain energy release rate can be controlled. Future experiments using the indentation method will employ displacement control instead of load control. Attempts will be made to obtain similar relations between the applied load and regions where moisture has a significant effect on crack propagation that the four-point bend test can measure.

Lane and Dauskardt have produced crack velocity versus crack driving energy data for TaN/SiO_2 interfaces. These plots show similar results to Wiederhorn's figure for bulk soda-lime glass. As previously seen, there are three distinct regions where changes in the slope are seen. Region I is only a function of the applied driving energy because the crack opening is too narrow for water molecules to reach the crack tip. In region II the crack velocity is strongly dependent on the environment and only slightly on the

applied crack driving force. For region III, crack velocity is no longer dependent on the environmental factors and is dominated by the applied driving force.

Generalizing the chemical rupture process, the interactions between the crack tip bonds B and environmental molecules A are:

$$nA + B \rightarrow B^* \tag{50},$$

where B^* denotes passage over the activation barrier into the ruptured state. This interaction facilitates lateral crack advance through one atomic spacing, with the n molecules of the depleted species A left associated with the broken bond on the new surfaces created.

For region I, where the driving energy drops and the crack velocity slows, the crack velocity is now controlled by bond rupture. With a smaller crack opening present, there will be a steric hindrance on water molecules and moisture concentration plays no role in crack advance:

$$v = v_0 \sinh\left[\frac{G_{tip} - 2\zeta}{\eta}\right] \tag{51},$$

where v_o and η are macroscopic crack growth parameters related to the local atomic and chemical environment, G_{tip} is the applied driving force at the crack tip and 2ζ is related to the chemical potential of the reacting species [53]:

$$2\zeta = N\left[\left(\mu_{B^*} - \mu_B\right) - x\left(\mu_A^\circ + RT \ln P_{H_2O}\right)\right] \tag{52},$$

where N is the number of bonds per unit area, μ_B* is the chemical potential of the reactive complex, μ_B is the chemical potential of the unreacted crack tip bonds, μ_A° is the chemical potential of the water molecules and R is the gas constant.

Predictions on the dependence of the crack velocity on moisture content in region II are as follows:

$$v = \frac{64 G a_0^3 P_{H2O}}{3\pi E a_0 \ln\left(\frac{I}{a_0}\right) x (2\pi m k T)^{\frac{1}{2}}} \quad (53),$$

where E is the Young's Modulus, I is the mean free path for the bulk gas, m is the mass of the diffusing species, P is the partial pressure of water vapor, x is the number of water molecules absorbed per bond, a_0 is the bond spacing, G is the mode I driving energy, T is the absolute temperature and k is Boltzmann's constant.

REFERENCES

1. A.A. Volinsky, N.R. Moody, W.W. Gerberich, *Interfacial Toughness Measurements for the Thin Films on Substrates*, Acta Mater. 50, pp. 441-466 (2002)

2. H. Jeong, S. Hata, A. Shimokohbe, *Microforming of Three-Dimensional Microstructures from Thin Film Metallic Glass*, J. MEMS 12, pp. 42-52 (2003)

3. X. Sun, Z. Jiang, S. Xin, Z. Yao, *Composition and Mechanical Properties of Hard Ceramic Coating Containing α-Al_2O_3 Produced by Microarc Oxidation on Ti-6Al-4V Alloy*, Thin Solid Films 471, pp. 194-199 (2005)

4. R. Bryce, H. Nguyen, P. Nakeeran, T. Clement, C. Haugen, R. Tykwinski, R. DeCorby, J. McMullin, *Polyamide-imide Polymer Thin Films for Integrated Optics*, Thin Solid Films 458, pp. 233-236 (2004)

5. T.R. Hsu, 'MEMS and Microsystems Design and Manufacture', McGraw-Hill, New York (2002)

6. M. Ohring, 'The Materials Science of Thin Films', Academic Press, London (1992)

7. http://www.pra.org.uk/technical/testingphysicalsurfacetension.htm#contact

8. D.M. Lipkin, D.R. Clarke, A.G. Evans, *Effect of Interfacial Carbon on Adhesion and Toughness of Gold-Sapphire Interfaces*, Acta Mater. 46, pp. 4835-4850 (1998)

9. G. Irwin, *Analysis of Stresses and Strains Near the End of a Crack Traversing a Plate*, J. Appl, Mech. 79, pp. 361-366 (1957)

10. B.R. Lawn, *An Atomistic Model of Kinetic Crack Growth in Brittle Solids*, J. Mat. Sci. 10, pp. 469-480

11. A.A. Griffith, *The Phenomena of Rupture and Flow in Solids*, Trans. R. Soc. Lond. pp. 163-198 (1920)

12. B. Lawn, *Fracture of Brittle Solids*, Cambridge University Press, Great Britain (1993)

13. J.W. Hutchinson, Z. Suo, *Mixed Mode Cracking in Layered Materials*, Adv. Appl. Mech. 29, pp. 63-191 (1992)

14. J. Dundurs, *Edge-Bonded Dissimilar Orthogonal Elastic Wedges Under Normal and Shear* Loading, J. Appl. Mech. 36, pp. 650-652 (1969)

15. M.R. Bayoumi, *The Mechanics and Mechanisms of Fracture in Stress Corrosion Cracking of Aluminum Alloys*, Eng. Frac. Mech. 54, pp. 879-889 (1996)

16. L. Grenet, *Mechanical Strength of Glass*, Bull. Soc. Enc. Industr. Nat. Paris 4, pp. 838-848 (1899)

17. S. Wiederhorn, *Influence of Water Vapor on Crack Propagation in Soda-Lime Glass*, Jour. Cer. Soc. 50, pp. 407-413 (1967)

18. V.P. Burolla, *Deterioration of the Silver/Glass Interface in Second Surface Solar Mirrors*, Sol. Ene. Mat. 3 pp. 117-126 (1980)

19. J. Vella, I. Adhihetty, K. Junker, A.A. Volinsky, *Mechanical Properties and Fracture Toughness of Organo-Silicate Glass (OSG) Low-k Dielectric Thin Films for Microelectronic Applications*, Inter. J. Fract. 119, pp. 487-499 (2003)

20. Y. Lin, J.J. Vlassak, T.Y. Tsui, A.J. McKerrow, *Environmental Effects on Subcritical Delamination of Dielectric and Metal Films from Organosilicate Glass (OSG) Thin Films*, MRS Symposium Proceedings (2004)

21. J.J. Vlassak, Y. Lin, T.Y. Tsui, *Fracture of Organosilicate Glass Thin Films: Environmental* Effects, Mat. Sci. Eng. A 391, pp. 159-174 (2005)

22. J. Moller, D. Reiche, M. Bobeth, W. Pompe, *Observation of Boron Nitride Thin Film Delamination Due to Humidity*, Sur. Coat. Tech. 150, pp. 8-14, (2002)

23. T. Tsuchiya, A. Inoue, J. Sakata, *Tensile Testing of Insulating Thin Film; Humidity Effect on Tensile Strength of SiO_2 Films*, Sen. Act. A 82, pp. 286-290 (2000)

24. W.R. Grove, Phil. Trans. 142, p. 87 (1852)

25. W.C. Oliver, G.M. Pharr, *An Improved Technique for Determining Hardness and Elastic Modulus using Load and Displacement Sensing Indentation Experiments*, J. Mat. Res. 7, pp. 1564-1580 (1992)

26. A.A. Volinsky, W.W. Gerberich, *Nanoindentation techniques for assessing mechanical reliability at the Nanoscale*, Mico. Elect. Eng. 69, pp. 519-527 (2003)

27. N. Yu, A. Polycarpou, T. Conry, *Tip-radius Effect in Finite Element Modeling of Sub-50 nm Shallow nanoindentation*, Thin Solid Films 450 pp. 295-303 (2003)

28. V. Gupta, A. Pronin, *New Technique to Measure the Toughness of Thin-Film Interfaces*, J. Amer. Ceram. Soc. 78 pp. 1397-1400 (1995)

29. M. Moon, K. Lee, K. Oh, J.W. Hutchinson, *Buckle Delamination on Patterned Substrates*, Acta Mat. In press, (2004)

30. J. Strong, *On the Cleaning of Surfaces*, Rev. Scient. Instr. 6, p.97 (1936)

31. P. Benjamin, C. Weaver, *Measurement of Adhesion of Thin Films*, Proc. Soc. London, 254, pp. 163-176 (1960)

32. S. Venkataraman, D. Kohlstedt, W.W. Gerberich, *Metal-Ceramic Interfacial Fracture Resistance using the Continuous Microscratch Technique*, Thin Solid Films, 223, pp. 69-275 (1993)

33. N.R. Moody, R. Hwang, S. Venka-Taraman, J. Angelo, D. Norwoods, W. Gerberich, *Adhesion and Fracture of Tantalum Nitride Films*, Acta Mater. 46, pp. 585-597 (1998)

34. D.B. Marshall, A.G. Evans, *Measurement of Adherence of Residually Stressed Thin Films by Indentation. I. Mechanics of Interface Delamination*, J. Appl. Phys. 56, pp. 2632-2638 (1984)

35. L. Katipelli, A. Agarwal, N. Dahotre, *Interfacial Strength of Laser Surface Engineered TiC Coating on 6061 Al using Four-Point Bend Test*, Mat. Sci. Eng. A. 289, pp. 34-40 (2000)

36. P. Charalambides, J. Lund, A.G. Evans, R. McMeeking, *A Test Specimen for Determining the Fracture Resistance of Bimaterial Interfaces*, J. Appl. Mech. 56, pp. 77-82 (1989)

37. M.D. Kriese, W.W. Gerberich, N.R. Moody, *Quantitative Adhesion Measures of MultilayerFilms: Part I Indentation Mechanics*, J. Mat. Res. 14, pp. 3007-3018 (1999)

38. A.A. Volinsky, *Experiments with In-situ Thin Film Telephone Cord Buckling Delamination Propagation*, Mat. Res. Soc. Symp. Proc. 749 (2003)

39. A. Lee, B. Clemens, W. Nix, *Stress Induced Delamination Methods for the Study of Adhesion of Pt Thin Films to Si*, Acta Mater. 52, pp. 2081-2093 (2004)

40. A.A. Volinsky, *The Role of Geometry and Plasticity in Thin, Ductile Film Adhesion*, Dissertation (2000)

41. G.G. Stoney, *The Tension of Metallic Films Deposited by Electrolysis*, Proc. Roy. Soc. London A 82, pp. 172-175 (1909)

42. P. Prevey, *X-Ray Diffraction Residual Stress Techniques*, Amer. Soc. Met. 10, pp. 380-392 (1986)

43. S.J. Cho, K.R. Lee, K.Y. Eun, J.H. Jeong, D. Kwon, *A Method of Determining the Elastic Properties of DLC Films*, Dia. Rel. Mat. 8, pp. 1067-1072 (1999)

44. M. Suzuki, T. Ohana, A. Tanaka, Dia. Rel. Mat. 13, pp. 2216-2220 (2004)

45. A.A. Volinsky, N. Tymiak, M.D. Kriese, W.W. Gerberich, *Quantitative Modeling and Measurement of Copper Thin Film Adhesion*, Mat. Res. Soc. Symp. Proc. 539, pp. 277-290 (1999)

46. N.I Tymiak, A.A. Volinsky, M.D. Kriese, S. Downs, W.W. Gerberich, *The Role of Plasticity in Bimaterial Fracture with Ductile Interlayers*, Met. Mat. Trans. A 31, pp. 863-871 (2000)

47. M.D. Kriese, N.R. Moody, W.W. Gerberich, *Effects of Annealing and Interlayers on the Adhesion Energy of Copper Thin Films to SiO_2/Si Substrates*, Acta Mat. 46, pp.6623-6630 (1998)

48. M.D. Kriese, D. Boismer, N.R. Moody, W.W. Gerberich, *Nanomechanical Fracture-Testing of Thin Films*, Eng. Frac. Mech. 61, pp. 1-20 (1998)

49. M.D. Kriese, W.W. Gerberich, *Quantitative Adhesion Measures of Multilayer Flms: Part II. Indentation of W/Cu, W/W, Cr/W*, J. Mater. Res. 14, pp. 3019- 3026 (1999)

50. A.A. Volinsky, P.J. Waters, J.D. Kiely, E. Johns, *Sub-Critical Telephone Cord Delamination Propagation*, Mat. Res. Soc. Symp. Proc. 854E, (2004)

51. A.A. Volinsky, D.C. Meyer, T. Leisegang, P. Paufler, *Fracture Patterns in Thin Films and Multilayers*, Mat. Res. Soc. Symp. Proc. 795, (2003)

52. R.W. Carpick, E.E. Flater, K. Sridharan, The Effect of Surface Chemistry and Structure on Nano-Scale Adhesion and Friction, Ply. Mat. Sci. Eng. 90 (2004)

53. M.W. Lane, J.M. Snodgrass, R.H. Dauskardt, *Environmental Effects on Interfacial Adhesion*, Microelectronics Reliability 41, pp. 1615-1624 (2001)

54. B.G. Willis, D.V. Lang, *Oxidaition Mechanism of Ionic Transport of Copper in SiO_2 Dielectrics*, Thin Solid Films 467, pp. 284-293 (2004)

55. J.J Perez-Bueno, R. Ramirez-Bon, Y.V. Vorobiev, F. Espinoza-Beltran, J. Gonzalez-Hernandez, Thin Solid Films 379, pp. 57-63 (2000)

56. J.B. Vella, S.M. Smith, A.A. Volinsky, I.S. Adhihetty, *Adhesion Quantification of Post-CMP Copper to Amorphous SiN Passivation by NanoIndentation*, Mat. Res. Soc. Symp. Proc. Vol. 649 (2001)

57. T.C. Wang, T.E. Hsieh, Y.L. Wang, Y.L.Wu, K.Y. Lo, C.W. Liu, K.W. Chen, Thin Solid Films 447, pp. 542-548 (2004)

58. W.W. Gerberich, A.A. Volinsky, N.I. Tymiak, *A Brittle to Ductile Transition in Adhered Thin Films*, Mat. Res. Soc. Symp. Proc. Vol. 594, pp. 351-364 (2000)

59. R. Tsu, J.W. McPherson, W.R. Mckee, *Leakage and Breakdown Reliability Issues Associated with Low-K Dielectrics in a Dual-Damascene Cu Process*, IEEE Inter. Rel. Phy. Symp. Proc. p. 348 (2000)

60. B. Audoly, B. Roman, A. Pocheau, *Secondary Buckling Patterns of a Thin Plat Under In-plane Compression*, Eur. Phys. J. B 27, pp. 7-10 (2002)

61. N. Nguyen, S. Wereley, 'Microfluidics', Artech House, London (2002)

62. A. Spence, S. Retterer, M. Isaacson, *Microfabricated Model Silicon Probes with Microfluidic, Channels for Drug Delivery*, NNUN Abstracts 2002/Biology & Chemistry, (2002)

63. Y. Li, M.N. Gulari, K.D. Wise, Proceedings of mTAS 2003 Seventh International Conference on Micro Total Analysis Systems, 2, pp. 931-934, (2003).

64. R. Zengerle, W. Geiger, M. Richter, J. Ulrich, S. Kluge, A. Richter, *Transient Measurements on Miniaturized Diaphram Pumps in Microfluid Systems*, Sen. Act. A 46, pp. 557-561 (1995)

65. F.G. Tseng, K.H. Lin, H.T. Hsu, C.C. Chieng, *A Surface-Tension-Driven Fluidic Network for Precise Enzyme Batch-Dispensing and Glucose Detection*, Sen. Act. A 111, pp. 107-117 (2004)

66. M.N. Kozicki, P. Maroufkhani, M. Mitkova, *Flow Regulation in Microchannels via Electrical Alteration of Surface Properties*, Superlattices and Microstructures, 34 pp. 467-473 (2003)

67. V. Ronesi, Y.W. Cheung, A. Hiltner, E. Baer, *Adhesion of Ethylene-Styrene Copolymers to Polyethylene in Microlayers*, J. App. Poly. Sci. 89, pp. 153-162 (2003)